

PILD: Physics-Informed Learning via Diffusion

Tianyi Zeng^{1*} Tianyi Wang^{2*} Jiaru Zhang¹ Zimo Zeng³ Feiyang Zhang⁴ Yiming Xu² Sikai Chen⁵
Yajie Zou⁴ Yangyang Wang⁴ Junfeng Jiao² Christian Clauzel² Xinbo Chen⁴

Abstract

Diffusion models have emerged as powerful generative tools for modeling complex data distributions, yet their purely data-driven nature limits applicability in practical engineering and scientific problems where physical laws need to be followed. This paper proposes Physics-Informed Learning via Diffusion (PILD), a framework that unifies diffusion modeling and first-principles physical constraints by introducing a virtual residual observation sampled from a Laplace distribution to supervise generation during training. To further integrate physical laws, a conditional embedding module is incorporated to inject physical information into the denoising network at multiple layers, ensuring consistent guidance throughout the diffusion process. The proposed PILD framework is concise, modular, and broadly applicable to problems governed by ordinary differential equations, partial differential equations, as well as algebraic equations or inequality constraints. Extensive experiments across engineering and scientific tasks including estimating vehicle trajectories, tire forces, Darcy flow and plasma dynamics, demonstrate that our PILD substantially improves accuracy, stability, and generalization over existing physics-informed and diffusion-based baselines.

1. Introduction

Diffusion models are a rising form of probabilistic generative models that learn data distributions by adding noise to data and training neural networks to reverse this process (Li et al., 2025). Through this iterative denoising mechanism, diffusion models have demonstrated strong performance across a wide range of domains, including computer

vision (Croitoru et al., 2023; Liu et al., 2024), temporal data modeling (Austin et al., 2021; Alcaraz & Strodthoff, 2022), and robust learning (Yoon et al., 2021; Blau et al., 2022). Owing to their rigorous mathematical interpretability grounded in probability theory, diffusion models exhibit a strong capability to learn complex data distributions (Yang et al., 2023). As a result, diffusion models have recently achieved state-of-the-art (SOTA) performance in both scientific machine learning (Luo et al., 2022; Lee et al., 2023) and practical engineering problems (Rixner & Koutsourelakis, 2021; Chen et al., 2023).

On the other hand, many scientific and engineering problems impose strict physical constraints governed by underlying differential equations (Lu et al., 2019). In such settings, training data are typically constructed either through numerical generations that enforce physical laws or through real-world measurements that inevitably contain noise (Raissi et al., 2019). Despite the aforementioned advances of diffusion models, the results sampled by standard diffusion models are not guaranteed to conform to physical laws, since they only learn the distribution characteristics at the data level (Huang et al., 2024). This limitation leads to physically invalid predictions or degraded performance, particularly in regimes involving highly complex dynamical systems.

Some research has explored integrating physical information into generative models, for instance, through enforcing physical priors through architectural constraints (Wang et al., 2025a) and physics-informed loss functions (Huang et al., 2024). However, most approaches introduce physical constraints in an ad-hoc imposed manner (Shan et al., 2025; Soni et al., 2025) or post-operation like distillation (Sanokowski et al., 2024), lacking a unified and generalizable framework that coherently integrates physical models with probabilistic generation. Recently, Bastek et al., 2024 and Baldan et al., 2025 represented an important step towards unifying physical models and data distributions within one diffusion or flow-matching framework, emerging as a crucial direction in physics-informed learning.

Based on this, we propose to embed physical laws such as partial differential equations (PDEs) directly into the diffusion model's training pipeline via a virtual residual observation, resolving inconsistencies between physical models

*Equal contribution ¹Shanghai Jiao Tong University, Shanghai, China ²The University of Texas at Austin, Austin, TX, USA ³Zhejiang University, Hangzhou, Zhejiang, China ⁴Tongji University, Shanghai, China ⁵University of Wisconsin-Madison, Madison, WI, USA. Correspondence to: Tianyi Wang <bonny.wang@utexas.edu>.

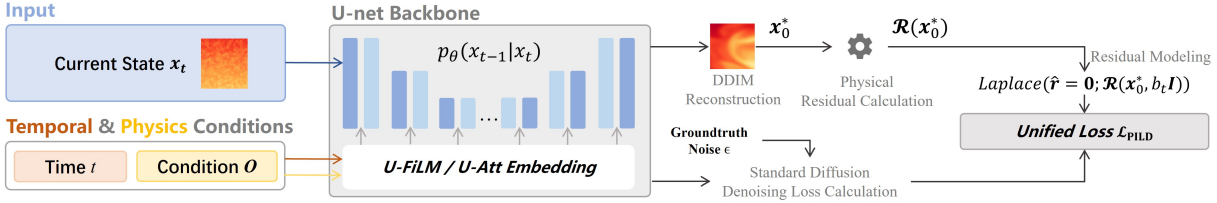


Figure 1. Overview of our PILD (Physics-Informed Learning via Diffusion) framework: The current state \mathbf{x}_t is fed into the network, while the current timestep t and condition O undergo conditional embedding via the ***U-FILM/U-Att module***. An estimation \mathbf{x}_0^* of original value is obtained by DDIM denoising. Modeling the virtual residual observable $\hat{\mathbf{r}}$ with Laplace distribution, we train the network under a ***unified loss*** with physics information.

and data distributions from first principles. Furthermore, to address insufficient guidance during diffusion (Jacobsen et al., 2025), we propose a conditional embedding module for explicit and pervasive physical guidance in training.

Building upon this, we introduce a Physics-Informed Learning via Diffusion (PILD) framework (Figure 1), which bridges the paradigms of Physics-Informed Neural Networks (PINNs) and diffusion-based generative modeling. The main contributions of this paper are as follows:

- We propose a diffusion framework that unifies physical models and data distributions. By introducing a virtual residual observation sampled from a Laplace distribution, we directly embed physical constraints into training, achieving a first-principles alignment between physical constraints and data-driven generation.
- We design a conditional embedding module that enables physical information to explicitly and pervasively guide the training workflow, improving controllability and physical fidelity in conditional generation.
- Our framework features a streamlined, modular architecture that generalizes to diverse scenarios. Extensive experiments across multiple engineering and scientific benchmark validate its effectiveness, robustness, and generalization capability.

2. Related Work

Diffusion models have demonstrated SOTA performance in generative tasks by learning to reverse a progressive noise-injection process applied to data (Hang et al., 2023). In particular, DDPM (Ho et al., 2020) formalized generation through a pair of Markov chains: a forward chain that perturbs data into noise, and a reverse chain that reconstructs samples from noise. Since then, diffusion models have achieved significant progress across various fields, especially in processing simple time series signals (Li et al., 2023; Yi et al., 2024). For instance, AEDM (Fu et al., 2025) applied diffusion models for denoising acoustic emission signals in concrete damage detection. Models like

DDIM (Song et al., 2020a) and EDM (Karras et al., 2022) offered expressive generative capabilities but remained limited when sampling with specific physical constraints.

Motivated by these limitations, recent work has attempted to incorporate physical priors into diffusion processes (Tee et al., 2024; Zhang & Zou, 2025; Yang & Zhang, 2025). Notably, PIDM (Bastek et al., 2024) unified denoising diffusion models with PINNs by incorporating PDE constraints into the training objective, reducing the residual errors of generated samples compared to the model proposed by Shu et al., 2023 and CoCoGen (Jacobsen et al., 2025). Building upon Shu et al., 2023's model, Pi-Fusion (Qiu et al., 2024) was designed for learning fluid dynamics based on diffusion models. DPS (Shi et al., 2024) introduced a novel computational technique for solving PDEs via PINN in the context of diffusion-based sampling. Inspired by Neural Network diffusion (Wang et al., 2024), Cheng & Alkhalifah, 2025 presented a latent diffusion-based approach to efficiently initialize PINNs for seismic wavefield modeling. Despite this progress, existing physics-informed diffusion models often suffer from physically inconsistent solutions and lack of deeply physical guided embedding. Therefore, the full potential of approaches integrating PINNs with diffusion models remains largely unexplored.

3. Preliminary

This section only includes the preliminary of diffusion models, while the preliminary of PINNs is provided in Appendix A.1. Diffusion models learn to gradually convert a sample of a simple prior to sample from an unknown data distribution $q(\mathbf{x}_0)$ (Song et al., 2020a). By adding Gaussian noise to sample data $\mathbf{x}_0 \sim q(\mathbf{x}_0)$, a forward process is defined as:

$$q(\mathbf{x}_{1:T}|\mathbf{x}_0) = \prod_{t=1}^T q(\mathbf{x}_t|\mathbf{x}_{t-1}), \quad (1)$$

$$q(\mathbf{x}_t|\mathbf{x}_{t-1}) = \mathcal{N}(\mathbf{x}_t; \sqrt{\alpha_t}\mathbf{x}_{t-1}, (1 - \alpha_t)\mathbf{I}),$$

where T is the number of forward steps and $\alpha_t \in (0, 1)$ is a parameter related to step t . So \mathbf{x}_t is expressed as a linear

combination of \mathbf{x}_0 and a noise variable ϵ :

$$\mathbf{x}_t = \sqrt{\alpha_t} \mathbf{x}_0 + \sqrt{1 - \alpha_t} \epsilon. \quad (2)$$

A reverse process is defined to generate new samples:

$$\begin{aligned} q(\mathbf{x}_{0:T}) &= p(\mathbf{x}_T) \prod_{t=1}^T q(\mathbf{x}_{t-1} | \mathbf{x}_t), \\ q(\mathbf{x}_{t-1} | \mathbf{x}_t) &= \mathcal{N}(\mathbf{x}_{t-1}; \boldsymbol{\mu}(\mathbf{x}_t, t), \boldsymbol{\Sigma}(\mathbf{x}_t, t)). \end{aligned} \quad (3)$$

We use $p_\theta(\mathbf{x}_0)$ generated by a neural network to approximate the distribution $q(\mathbf{x}_0)$, which is defined as:

$$p_\theta(\mathbf{x}_0) = \int p_\theta(\mathbf{x}_{0:T}) d\mathbf{x}_{1:T}, \quad (4)$$

where $p_\theta(\mathbf{x}_{0:T}) := p_\theta(\mathbf{x}_T) \prod_{t=1}^T p_\theta^{(t)}(\mathbf{x}_{t-1} | \mathbf{x}_t)$ and $\mathbf{x}_1, \mathbf{x}_2, \dots, \mathbf{x}_T$ are latent variables in the same sample space as \mathbf{x}_0 . The network aims to estimate the mean value $\boldsymbol{\mu}_\theta$, while the covariance is fixed to:

$$\boldsymbol{\Sigma}(\mathbf{x}_t, t) = \frac{1 - \bar{\alpha}_{t-1}}{1 - \bar{\alpha}_t} \beta_t \mathbf{I} = B_t \mathbf{I}, \quad (5)$$

where $\bar{\alpha}_t = \prod_{i=1}^t \alpha_i$, and $\beta_t = 1 - \alpha_t$.

The parameters θ are trained to fit $q(\mathbf{x}_0)$ by maximizing a variational lower bound (Song et al., 2020a):

$$\begin{aligned} \max_{\theta} \mathbb{E}_{q(\mathbf{x}_0)} [\log p_\theta(\mathbf{x}_0)] &\leq \\ \max_{\theta} \mathbb{E}_{q(\mathbf{x}_0, \mathbf{x}_1, \dots, \mathbf{x}_T)} [\log p_\theta(\mathbf{x}_0; T) - \log q(\mathbf{x}_{1:T} | \mathbf{x}_0)], \end{aligned} \quad (6)$$

where $q(\mathbf{x}_{1:T} | \mathbf{x}_0)$ is inference distribution over latent variables $\mathbf{x}_1, \mathbf{x}_2, \dots, \mathbf{x}_T$. Estimating $\boldsymbol{\mu}_\theta$ is obvious, but alternative parameterizations are possible. According to the Bayes' theorem (Efron, 2013), the mean value $\boldsymbol{\mu}_t$ at time step t is then given by:

$$\boldsymbol{\mu}_t(\mathbf{x}_t, \epsilon_t) = \frac{\sqrt{\alpha_t}(1 - \bar{\alpha}_{t-1})}{1 - \bar{\alpha}_t} \mathbf{x}_t + \frac{\sqrt{\bar{\alpha}_{t-1}}\beta_t}{1 - \bar{\alpha}_t} \mathbf{x}_0, \quad (7)$$

where ϵ_t is the applied Gaussian noise. During training, \mathbf{x}_t is known, so ϵ_t is obtainable by predicting $\boldsymbol{\mu}_\theta$. Furthermore, Ho et al., 2020 simplified the training loss as:

$$\mathcal{L}_n(\theta) := \mathbb{E}_{t, \mathbf{x}_0, \epsilon} [||\epsilon - \epsilon_\theta(\sqrt{\alpha_t} \mathbf{x}_0 + \sqrt{1 - \alpha_t} \epsilon, t)||^2], \quad (8)$$

where t is uniform from 1 to T , ϵ_θ is the noise predicted by network with parameters θ . So, we can train the model to generate the clean signal \mathbf{x}_0 .

4. Methodology

The objective of this work is to enhance the physical consistency of samples generated by diffusion models. Standard

data-driven generative models typically learn a data distribution from samples drawn from a target system, but they do not explicitly capture the underlying physical laws (e.g., residual $\mathcal{R}(\mathbf{x}_0) = 0$) (Ghanem et al., 2024). To address this, we directly incorporate the governing physical equations into the optimization objective and embed observational data as conditioning inputs, thereby enabling deeply physics-informed guidance throughout training.

4.1. Physics-Informed Diffusion Training Framework

Our method assumes access to training data sampled either from simulators or real-world measurements. This assumption is fundamental: if training data contain substantial errors or fundamentally violate the objective physical laws, the resulting data distribution will inherently fail to satisfy physical constraints, thereby misleading the learning process. In practice, while data collected from real-world systems may contain noise or outliers, they generally conform to correct physical principles in a probabilistic sense (e.g., Newtonian mechanics), rendering it suitable for physics-informed learning. Consequently, system identification lies outside the scope of this work.

Our approach hinges on the ability to estimate the clean, original data $\mathbf{x}_0 \sim q(\mathbf{x}_0)$ from any noisy state \mathbf{x}_t using the network's noise prediction ϵ_θ under condition \mathbf{O} . According to Equation (6), the objective of the training procedure is to maximize the variational lower bound. Therefore, the data-driven part of the training objective is expressed as:

$$\arg \max_{\theta} \mathbb{E}_{\mathbf{x}_0 \sim q(\mathbf{x}_0)} [\log p_\theta(\mathbf{x}_0 | \mathbf{O})]. \quad (9)$$

For the physics-informed component of the training objective, accounting for potential noise or outliers in the training data (from either simulators or real systems), we introduce a virtual residual observation $\hat{\mathbf{r}} = \mathbf{0}$ sampled from a Laplace distribution (Rixner & Koutsourelakis, 2021), which is inherently more robust to outliers (Kotz et al., 2012):

$$q_{\mathcal{R}}(\hat{\mathbf{r}} | \mathbf{x}_0) = \text{Laplace}(\hat{\mathbf{r}}; \mathcal{R}(\mathbf{x}_0), \sigma \mathbf{I}). \quad (10)$$

We adopt a probabilistic modeling perspective to render the residual constraint compatible with the generative model's optimization framework: as $\sigma \rightarrow 0$, the distribution $q_{\mathcal{R}}(\hat{\mathbf{r}} | \mathbf{x}_0)$ converges to $\mathcal{R}(\mathbf{x}_0)$. Thus, the optimization objective here is probabilistically consistent with that of classical PINNs. To drive the residual toward 0, we introduce virtual likelihood $p_\theta(\hat{\mathbf{r}})$ as:

$$\begin{aligned} p_\theta(\hat{\mathbf{r}}) &= \int p_\theta(\hat{\mathbf{r}}, \mathbf{x}_0) d\mathbf{x}_0 = \int q_{\mathcal{R}}(\hat{\mathbf{r}} | \mathbf{x}_0) p_\theta(\mathbf{x}_0) d\mathbf{x}_0 \\ &= \mathbb{E}_{\mathbf{x}_0 \sim p_\theta(\mathbf{x}_0 | \mathbf{O})} [q_{\mathcal{R}}(\hat{\mathbf{r}} | \mathbf{x}_0)]. \end{aligned} \quad (11)$$

Maximizing its log-likelihood yields the following optimization objective:

$$\begin{aligned} \arg \max_{\theta} \mathbb{E}_{\hat{\mathbf{r}}} [\log p_{\theta}(\hat{\mathbf{r}})] = \\ \arg \max_{\theta} \mathbb{E}_{\mathbf{x}_0 \sim p_{\theta}(\mathbf{x}_0 | \mathcal{O})} [\log q_{\mathcal{R}}(\hat{\mathbf{r}} = \mathbf{0} | \mathbf{x}_0)]. \end{aligned} \quad (12)$$

While our physics-informed term can be interpreted probabilistically as a virtual likelihood that mirrors the residual loss in PINNs (Raissi et al., 2019), our objective fundamentally differs: we aim not to solve a PDE, but to learn a data distribution enriched with physical priors, ensuring that generated samples are both statistically representative and physically plausible. Subsequently, the overall training objective is interpreted as optimizing a joint log-likelihood over both the data samples and virtual residual observables:

$$\begin{aligned} \arg \max_{\theta} \{ \mathbb{E}_{\mathbf{x}_0 \sim q(\mathbf{x}_0)} [\log p_{\theta}(\mathbf{x}_0 | \mathcal{O})] + \\ \mathbb{E}_{\mathbf{x}_0 \sim p_{\theta}(\mathbf{x}_0 | \mathcal{O})} [\log q_{\mathcal{R}}(\hat{\mathbf{r}} = \mathbf{0} | \mathbf{x}_0)] \}. \end{aligned} \quad (13)$$

The training objective of denoising diffusion models can be rigorously interpreted as learning the score function $\nabla_{\mathbf{x}_t} \log p_t(\mathbf{x}_t)$ within the framework of score-based generative models (Song et al., 2020b). Crucially, as detailed in Appendix A.2, when the physics-informed term is incorporated as a virtual residual likelihood, the resulting joint objective remains theoretically consistent under this score-based perspective: the optimal score model simultaneously maximizes the data log-likelihood and enforces physical consistency, without compromising its ability to recover samples from the true data distribution $q(\mathbf{x}_0)$ (Bastek et al., 2024). This justifies our formulation in Equation (13) as a principled fusion of data-driven learning and physical priors. Since Equation (13) requires sampling from both $p_{\theta}(\mathbf{x}_0 | \mathcal{O})$ and $q(\mathbf{x}_0)$, directly optimizing this joint likelihood is computationally challenging (Ho et al., 2020). Therefore, we adopt DDIM (Song et al., 2020a) for accelerated sampling. The detailed introduction of Laplace distribution is illustrated in Appendix A.3.

To ensure clean denoising of the diffusion model as $t \rightarrow 0$, we first modulate $q_{\mathcal{R}}(\hat{\mathbf{r}} | \mathbf{x}_0^*)$ using a variance $b_t = B_t/c$ informed by the sampled data as:

$$q_{\mathcal{R}}(\hat{\mathbf{r}} | \mathbf{x}_0^*) = \prod_{t=1}^T \text{Laplace}(\hat{\mathbf{r}}; \mathcal{R}(\mathbf{x}_0^*), b_t \mathbf{I}), \quad (14)$$

where $\mathbf{x}_0^* = \text{DDIM}[\mathbf{x}_t]$, $c > 0$ is a hyperparameter effectively dictating the strength of the physical penalty, B_t is the fixed variance of denoising process which has been mentioned in Equation (5). The adoption of DDIM sampling for \mathbf{x}_0^* estimation is a core strategy to mitigate the Jensen gap (Gao et al., 2017), which arises from the fundamental inequality $\mathcal{R}(\mathbb{E}[\mathbf{x}_0 | \mathbf{x}_t]) \neq \mathbb{E}[\mathcal{R}(\mathbf{x}_0) | \mathbf{x}_t]$ for non-linear physical residual operators \mathcal{R} . Unlike mean estimation (where

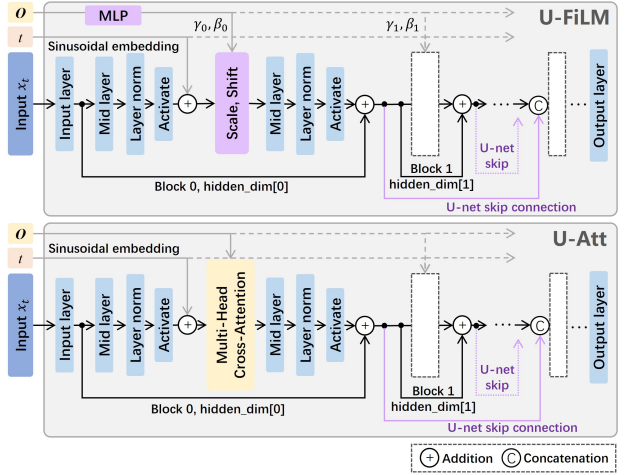


Figure 2. U-FiLM and U-Att condition embedding structure.

$\hat{x}_0 = \mathbb{E}[\mathbf{x}_0 | \mathbf{x}_t]$ only captures the first moment of the posterior), DDIM generates an actual sample from the conditional distribution $p(\mathbf{x}_0 | \mathbf{x}_t, \mathcal{O})$, which preserves the full distributional characteristics of \mathbf{x}_0 and reduces the bias between $\mathcal{R}(\mathbf{x}_0^*)$ and $\mathcal{R}(\mathbf{x}_0)$ (Bastek et al., 2024). This aligns with the consistency proof in Appendix A.2. Additionally, we present a gate function $G(t) = \log(1 + \frac{T}{1+t})$, which enlarges physical penalties when t is smaller. The justification and ablation for $G(t)$ is provided in Appendix A.4 and A.8.6.

During the optimization of the variational lower bound, p_{θ} gradually converges to q . Then, the total loss $\mathcal{L}_{\text{PILD}}$ is formulated under the same expectation over the combined objectives (a detailed proof is provided in Appendix A.5), ensuring an elegant integration of data and robust physics:

$$\begin{aligned} \mathcal{L}_{\text{PILD}}(\theta) = \mathbb{E}_{t \sim [1, T], \mathbf{x}_0 \sim q(\mathbf{x}_0), \mathcal{O}, \epsilon \sim \mathcal{N}(0, \mathbf{I})} \\ \left[\lambda_t \|\epsilon - \epsilon_{\theta}\|^2 + \frac{1}{b_t} G(t) \|\mathcal{R}(\mathbf{x}_0^*)\|_1 \right], \end{aligned} \quad (15)$$

where λ_t is a time-dependent Min-SNR weighting (Hang et al., 2023) that naturally balances the denoising objective across different noise levels, fundamentally arising from the score matching equivalence for maximizing data likelihood.

This framework is also applicable to other types of constraints and the details with toy experiment are illustrated in Appendix A.7.

4.2. Conditional Embedding

To ensure deep embedding of the condition \mathcal{O} during training, we propose two conditioning strategies that share a common interface and can be seamlessly integrated into the diffusion framework according to different requirements, which are shown in Figure 2. The first strategy is a U-Net-based Feature-wise Linear Modulation, denoted as U-FiLM; the second employs a Multi-Head Cross-Attention-based

embedding mechanism, denoted as U-Att. Input of the module is \mathbf{x}_t , with conditional inputs \mathbf{O} and the time step t .

In U-FiLM, we integrate it into the U-Net backbone using FiLM (Perez et al., 2018). This mechanism transforms the static conditional variables into a dynamic function modulator that operates on the hidden representations within the network. The condition \mathbf{O} is first processed by a multilayer perceptron (MLP) to generate a set of parameters (γ_i, β_i) for i th residual block; these parameters modulate the features within the corresponding block as follows:

$$FiLM(\mathbf{h}_i; \gamma_i, \beta_i) = (1 + \gamma_i) \odot \mathbf{h}_i + \beta_i, \quad (16)$$

where \mathbf{h}_i is the input feature of *Scale*, *Shift* block, and \odot is element-wise multiplication. Here, we adjust the coefficient to $(1 + \gamma_i)$ instead of γ_i mentioned by Perez et al., 2018. Practical experience shows that this modification stabilizes the training in early iterations and ensures proper gradient backpropagation.

In U-Att, the condition \mathbf{O} is directly fed into the Multi-Head Cross-Attention block, thereby embedding the control condition into the training process.

It should be noted that both mechanisms serve as valid forms of conditional embedding, exhibiting distinct performance characteristics depending on the dimensionality of the target data (Chi et al., 2023). For one-dimensional targets (e.g., scattered points or univariate time series), both achieve strong performance, with U-FiLM offering reduced training time due to its simpler architecture. For multi-dimensional targets (e.g., 2D fields), U-Att demonstrates superior performance by effectively capturing high-dimensional inter-feature dependencies.

Moreover, the neural network within the aforementioned framework can be either MLP-based or convolutional neural network (CNN)-based, depending on the dimensionality of the data being processed. We will demonstrate both settings in the experimental section.

Furthermore, the framework remains applicable to unconditional generation (without \mathbf{O}). Since the modules processing \mathbf{O} are connected in series along the residual main branch in the original U-Net structure, they can be removed to enable unconditional generation, which is fully compatible with PILD’s framework.

4.3. Diffusion Inference and Sampling

Once the model ϵ_θ has been trained by minimizing $\mathcal{L}_{\text{PILD}}$, it can be employed as a conditional generator to sample new solutions. Instead of modeling the joint distribution $p(\mathbf{x}_0, \mathbf{O})$, our model directly approximates conditional distribution $p(\mathbf{x}_0|\mathbf{O})$. This formulation allows the model to generate physically consistent samples \mathbf{x}_0 conditioned on input observations \mathbf{O} without the computational overhead of

Algorithm 1 PILD Model DDIM Sampling

- 1: **Input:** Trained noise prediction network ϵ_θ , condition \mathbf{O} , total diffusion steps T , variance schedule $\bar{\alpha}_t$ (cumulative product of $\alpha_t = 1 - \beta_t$).
- 2: **Output:** Generated sample \mathbf{x}_0 .
- 3: Draw initial noise sample $\mathbf{x}_T \sim \mathcal{N}(\mathbf{0}, \mathbf{I})$.
- 4: **Step 1: Sample \mathbf{x}_1 from \mathbf{x}_T via DDIM**
- 5: Predict noise for timestep T : $\hat{\epsilon} = \epsilon_\theta(\mathbf{x}_T, \mathbf{O}, T)$
- 6: Estimate clean sample from \mathbf{x}_T : $\hat{\mathbf{x}}_0^{(T)} = \frac{1}{\sqrt{\bar{\alpha}_T}} (\mathbf{x}_T - \sqrt{1 - \bar{\alpha}_T} \hat{\epsilon})$
- 7: Compute intermediate sample \mathbf{x}_1 using DDIM formula:
- 8: $\mathbf{x}_1 = \sqrt{\bar{\alpha}_1} \hat{\mathbf{x}}_0^{(T)} + \sqrt{\frac{1 - \bar{\alpha}_1}{1 - \bar{\alpha}_T}} \cdot (\mathbf{x}_T - \sqrt{\bar{\alpha}_T} \hat{\mathbf{x}}_0^{(T)})$
- 9: **Step 2: Generate final \mathbf{x}_0 from \mathbf{x}_1**
- 10: Predict noise for timestep 1: $\hat{\epsilon}' = \epsilon_\theta(\mathbf{x}_1, \mathbf{O}, 1)$
- 11: Estimate clean sample (final output) from \mathbf{x}_1 :
- 12: $\mathbf{x}_0 = \frac{1}{\sqrt{\bar{\alpha}_1}} (\mathbf{x}_1 - \sqrt{1 - \bar{\alpha}_1} \hat{\epsilon}')$

inferring the observations themselves. The two-step DDIM has also been shown to significantly accelerate sampling while ensuring accuracy (Bastek et al., 2024); thus, we adopt the two-step DDIM for sampling in Algorithm 1.

By manipulating the input conditions \mathbf{O} , we can perform “what-if” analyses and generate corresponding solution profiles that are guaranteed to be both diverse (due to the stochastic nature of \mathbf{z}) and physically consistent (due to the training objective and conditional embedding). This generative capability enables not only point predictions but also the characterization of solution uncertainty by generating an ensemble of samples for a fixed condition.

5. Experiments

To verify the role of PILD in both providing stable physical guidance and improving physical consistency of training, we conduct experiments on four datasets, covering applications in engineering systems and scientific machine learning. Due to space limitations, details for each experiment, baseline methods and ablations are provided in the Appendix A.6 and A.8; only key settings and results are presented here. In the tables, the bold data is the best one and the underlined one has the second best performance.

5.1. Vehicle Tracking

Vehicle tracking requires a vehicle dynamic model to predict the future state. The Ackerman steering model (Mitchell et al., 2006) includes longitudinal, lateral, and yaw motions, which can be expressed as:

$$[x_{t+1}, y_{t+1}, \psi_{t+1}, v_{x_{t+1}}]^\top = \mathcal{F}([x_t, y_t, \psi_t, v_{x_t}]^\top, [\theta, \dot{u}])^\top, \quad (17)$$

where $[x, y, \psi, v]^\top$ is the vehicle state vector (x coordinate, y coordinate, yaw angle, forward velocity), $[\theta, u]^\top$ is the control vector (θ steering angle, u acceleration), and the system transfer equation is denoted as \mathcal{F} .

This task aims to predict the vehicle state at the next time step based on its state and control input at the current time step. The methods used for comparison include **EKF** (Ribeiro, 2004), **FCN** (Long et al., 2015), **ResNet** (He et al., 2016), **PINN-FCN** (Long et al., 2022), **PINN-ResNet** (Long et al., 2022), **B-PINN** (Pensoneault & Zhu, 2024), **LSTM-RNN** (Ip et al., 2021), **LSTM-GA** (Zeng et al., 2023), **DDPM** (Ho et al., 2020), and **PIDM** (Bastek et al., 2024). The experiments are performed on a vehicle driving dataset (Wang et al., 2025b) with two scenarios: downtown and rural area driving, respectively. It should be noted that the experimental setup differs from conventional settings in that trajectory points prediction is performed incrementally to evaluate the accumulation of prediction errors over time.

The quantitative results are presented in Table 1. Due to space constraints, the results with measurement variance are presented in Table 9 of Appendix A.8.1. We select one trajectory for each scenario for demonstration in Figure 3. Basic methods and LSTM-based methods perform poorly on the mixed-vehicle dataset, as they struggle to discern that the variations in data characteristics stem from differing physical model parameters. PINNs are also constrained by fixed physical models, limiting their adaptability. Consequently, both categories exhibit significant error accumulation over time, leading to substantial trajectory deviations, as shown in Figure 3. In contrast, diffusion-based methods, owing to their strong generative capacity, effectively capture the underlying data distribution, resulting in consistently lower prediction errors. It is worth noting that in the downtown scenario, PIDM exhibits a smaller yaw angle error than PILD. This can be attributed to the rapid variations of the yaw angle in this scenario, where the error distribution in certain cases may align more closely with a Gaussian distribution rather than the Laplace distribution. However, across other metrics and practical scenarios, the experimental results still validate the rationality of our Laplace modeling.

5.2. Tire Forces

The measurement of vehicle dynamic tire forces has long been a focal topic within the automotive community, which directly govern both safety and dynamic stability of vehicles (Zeng et al., 2024). The vertical tire force serves as the foundation for tire forces in other directions. Therefore, it is typically of primary interest and can be expressed as:

$$\frac{\partial F_z(t, T)}{\partial t} = \mathcal{F}(\mathcal{O}), \quad (18)$$

where \mathcal{O} is the set of sensors' data, t is time, T is tire temperature, and \mathcal{F} denotes the tire force calculation term.

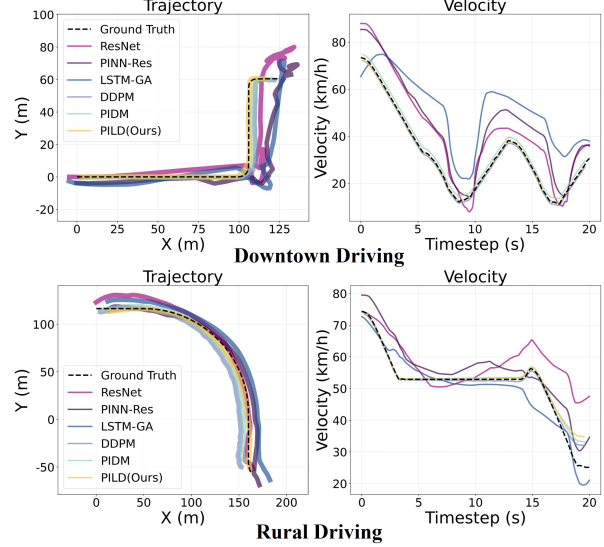


Figure 3. Experiment results on tracking tasks.

Table 1. Quantitative results on tracking tasks.

Method	Downtown Driving			Rural Driving		
	$e_{x\&y\downarrow}$	$e_{\psi\downarrow}$	$e_{v_x\downarrow}$	$e_{x\&y\downarrow}$	$e_{\psi\downarrow}$	$e_{v_x\downarrow}$
EKF	6.602	6.930	5.476	6.179	6.241	5.512
FCN	9.567	7.977	14.284	9.623	6.606	10.972
ResNet	9.236	6.899	9.094	5.517	10.361	9.315
PINN-FCN	8.824	14.488	17.287	8.279	10.349	15.251
PINN-ResNet	5.923	9.753	11.286	3.729	9.134	8.248
B-PINN	5.867	6.597	10.563	6.034	6.511	9.656
LSTM-RNN	8.953	10.199	11.298	9.643	8.831	8.168
LSTM-GA	9.019	6.579	8.442	9.005	5.994	10.837
DDPM	9.653	6.109	4.317	4.697	7.138	4.936
PIDM	4.845	4.733	5.671	4.293	5.874	4.061
PILD (Ours)	4.796	5.391	3.048	3.562	5.837	3.033

We evaluate our approach on a racing car chassis dynamic dataset (Zeng et al., 2023) with three sets of working conditions, including aggressive, sporty, and smooth driving. The methods used for comparison include **EKF** (Ribeiro, 2004), **FCN** (Long et al., 2015), **ResNet** (He et al., 2016), **PINN-FCN** (Long et al., 2022), **PINN-ResNet** (Long et al., 2022), **B-PINN** (Pensoneault & Zhu, 2024), **LSTM-RNN** (Ip et al., 2021), **LSTM-GA** (Zeng et al., 2023), **DDPM** (Ho et al., 2020), and **PIDM** (Bastek et al., 2024).

The quantitative results are presented in Table 2. The results with variance are also provided in Table 10 of Appendix A.8.2. We select three methods for demonstration in Figure 4, more samples are provided in Figure 11 in Appendix A.8.2. Since all the needed sensors are installed in chassis, the collected data contain significant noise. So, we conducted ablation studies on whether to apply denoising to the input. As presented in Appendix A.8.6, the experimental results not only highlight the importance of data prepro-

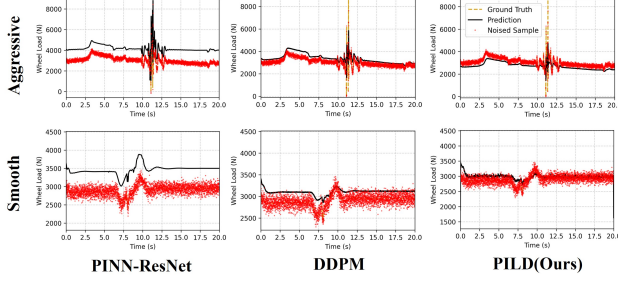


Figure 4. Samples of tire force estimation experiments on PINN, DDPM and PILD (Ours).

Table 2. Quantitative results on tire force estimation tasks.

Method	Aggressive $e_F \downarrow$	Smooth $e_F \downarrow$	Sporty $e_F \downarrow$
EKF	1008.127	597.363	716.543
FCN	1257.633	601.559	794.780
ResNet	1121.367	585.561	647.976
PINN-FCN	1012.849	551.508	654.644
PINN-ResNet	994.783	642.110	653.944
B-PINN	1002.531	598.617	661.279
LSTM-RNN	1302.589	720.567	788.163
LSTM-GA	1150.434	582.840	642.638
DDPM	980.328	560.796	660.897
PIDM	988.642	579.546	630.543
PILD (Ours)	958.578	520.631	607.274

cessing but also demonstrate the robustness of our method. Different types of vehicles have totally different chassis dynamics, posing significant challenges to physical consistency. While the EKF is a classical traditional method for addressing such problems, it underperforms learning-based approaches when the dataset includes multiple vehicle models and inherent noise. Diffusion-based methods achieve superior performance, with physics-informed diffusion models delivering even better results. Furthermore, the results revalidate the superiority of Laplace-distributed modeling in solving practical engineering problems.

5.3. Darcy Flow

Modeling subsurface flow requires solving a parameterized partial differential equation governed by Darcy's law (Hubert, 1956). The relationship between the permeability field $k(\mathbf{x})$ and the resulting pressure field $p(\mathbf{x})$ is expressed as:

$$-\nabla \cdot (k(\mathbf{x}) \nabla p(\mathbf{x})) = f(\mathbf{x}), \quad \mathbf{x} \in \Omega, \quad (19)$$

where Ω denotes the spatial domain, $f(\mathbf{x})$ is a known source term, and appropriate boundary conditions are imposed on $\partial\Omega$. The model's output consists of two channels, corresponding to the permeability field k and the pressure field p , and the PDE residual $\mathcal{R}(k, p) = -\nabla \cdot (k \nabla p) - f$ is incorporated directly into the training objective to enforce physical consistency.

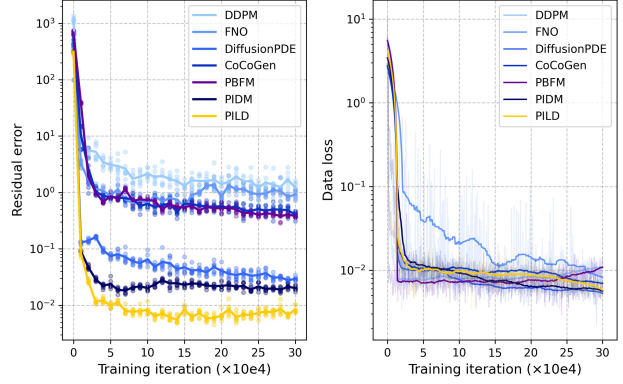


Figure 5. Evaluation of residual error and data loss of Darcy flow.

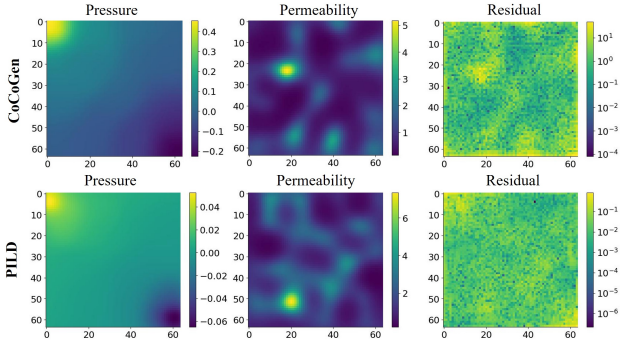


Figure 6. Samples of Darcy flow generation experiments on CoCoGen and PILD (Ours).

This task is to generate pressure and permeability fields that satisfy the Darcy's laws. The Darcy flow dataset used in our experiments is from Jacobsen et al., 2025. The methods used for comparison include **DDPM** (Ho et al., 2020), **FNO** (Li et al., 2020), **DiffusionPDE** (Huang et al., 2024), **CoCoGen** (Jacobsen et al., 2025), **PBFM** (Baldan et al., 2025), and **PIDM** (Bastek et al., 2024).

The testing data loss and residual error are shown in Figure 5. In terms of physical residual error, PILD achieves a substantial reduction compared to other baselines, even outperforming PIDM by approximately 50%. This validates the effectiveness of our Laplace-distributed residual modeling. Regarding data loss, as the Darcy flow task is unconditional, the generation is solely constrained by the unified loss, yielding comparable data loss to other methods. PILD reduces physical loss while preserving this data loss performance, validating its effectiveness without sacrificing data consistency for physical loss minimization. We select several samples for demonstration in Figure 12 in Appendix A.8.3. More samples are provided in Figure 12 in Appendix A.8.3.

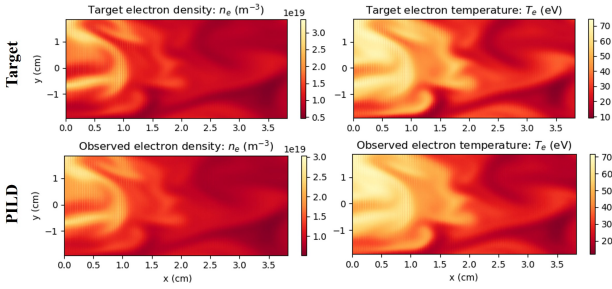


Figure 7. Samples of plasma dynamics prediction experiments on PILD (Ours).

Table 3. Quantitative results on plasma dynamics prediction.

Method	Density error (10^{19})	Temperature error
PINN	0.531 ± 0.095	5.292 ± 0.538
DDPM	0.122 ± 0.020	1.766 ± 0.284
FNO	0.153 ± 0.046	1.609 ± 0.258
DiffusionPDE	0.112 ± 0.014	0.728 ± 0.067
PBFM	0.127 ± 0.025	1.293 ± 0.116
PIDM	0.107 ± 0.012	0.831 ± 0.061
PILD (Ours)	0.074 ± 0.011	0.451 ± 0.055

5.4. Plasma Dynamics

Modeling edge plasma turbulence requires solving the drift-reduced Braginskii equations (Mathews et al., 2021), a system of nonlinear PDEs governing the evolution of key plasma fields. Of particular interest are the electron density $n(\mathbf{x}, t)$ and the electron temperatures $T_e(\mathbf{x}, t)$, whose normalized logarithmic forms evolve according to:

$$\frac{d \ln n}{dt} = \mathcal{S}_n(n, \phi, T_e, \dots), \quad \frac{d \ln T_e}{dt} = \mathcal{S}_{T_e}(n, T_e, \phi, \dots), \quad (20)$$

where \mathcal{S}_n and \mathcal{S}_{T_e} denote the right-hand-side source terms derived from the full two-fluid plasma model, which include effects such as advection, parallel heat conduction, and collisional coupling, and ϕ is electrostatic potential.

In our experiment, the PILD is trained to jointly predict the fields of n and T_e based on observations including ϕ and other parameters. We use the dataset from Mathews et al., 2021, and compare our method against the following methods: **PINN** (Mathews et al., 2021), **DDPM** (Ho et al., 2020), **FNO** (Li et al., 2020), **DiffusionPDE** (Huang et al., 2024), **PBFM** (Baldan et al., 2025), and **PIDM** (Bastek et al., 2024).

Quantitative results are reported in Table 3. A representative sample is visualized in Figure 7, and more samples are provided in Figure 13 in Appendix A.8.4. It can be observed that methods incorporating physical information demonstrate clear advantages in solving complex PDE problems. DDPM, which lacks explicit physics integration, exhibits

Table 4. Ablation studies on core modules.

Method	Plasma Dynamics Density error \downarrow	Tire Force $e_F \downarrow$
w/ U-FiLM	0.082	695.494
w/ U-Att	0.074	699.316
w/ Gating function	0.074	695.494
w/o Gating function	0.088	720.106
Laplace modeling	0.074	695.494
Gaussian modeling	0.105	839.167
Physical $c = 0$	0.097	734.007
Physical $c = 10^{-3}$	0.186	856.376
Physical $c = 10^{-4}$	0.112	695.494
Physical $c = 10^{-5}$	0.074	726.981
Diffusion Steps=20	0.095	820.793
Diffusion Steps=50	0.089	702.538
Diffusion Steps=100	0.074	695.494

larger errors overall. PINN, struggles to balance the physics loss with data distribution in generative tasks, leading to inferior performance compared to diffusion-based methods.

5.5. Ablation Studies

We conduct ablation studies on several core components and hyperparameters of PILD, evaluating on the Plasma Dynamics and Tire Force scenarios (Here the Tire Force error is the mean value of the three conditions mentioned above). Results are presented in Table 4. We observe that when handling high-dimensional data, U-Att outperforms U-FiLM because cross-attention better captures inter-feature dependencies, though U-FiLM is more computationally efficient (see Appendix A.8.6). For modeling the virtual residual, the Laplace distribution is superior to the Gaussian distribution, particularly on noisy real-world datasets, as it imposes a stronger penalty on outliers. The weight of the physics loss must be carefully tuned. Excessive values hinder the model from learning data-specific physical features, while small values weaken physical consistency. Diffusion steps impact prediction accuracy, though excessively large values significantly increase training cost. Moreover, we also conducted ablation studies on input **with or without denoising process**, **different kinds of gating functions** and **training cost**, which are demonstrated in Appendix A.8.6.

6. Conclusion

This paper proposes the PILD framework to enhance the physical consistency of diffusion-based generative models. Within the PILD framework, we introduce a virtual residual observation sampled from a Laplace distribution to bridge the physics loss and the data loss, thereby establishing a unified training objective grounded in first principles.

A dedicated physics-informed embedding module enables deep integration of physical knowledge into the training process. Experiments on multiple benchmarks demonstrate the effectiveness of the proposed method.

This paper also introduces a few interesting open problems. For example, PILD adopts DDIM sampling to mitigate the impact of Jensen gap, while it only alleviates the gap rather than fundamentally eliminating it from a mathematical perspective. While some methods attempt to eliminate the gap via distillation or post-training, they introduce additional steps to the original workflow, resulting in redundant and inelegant operations. Therefore, exploring alternative mathematically rigorous approaches to fully eliminate the Jensen gap constitutes a key direction for future research.

Acknowledgments

The authors have stated that they have no potential conflicts of interest of this article and they did not receive any funding for this work.

Impact Statement

The aim of this paper is to promote communication and research in the field of machine learning and to promote its application in cross-disciplines such as engineering and scientific fields. We do not think the possible social implications of this study need to be particularly emphasized here.

References

Adam, K. D. B. J. et al. A method for stochastic optimization. *arXiv preprint arXiv:1412.6980*, 1412(6), 2014.

Aithal, S. K., Maini, P., Lipton, Z., and Kolter, J. Z. Understanding hallucinations in diffusion models through mode interpolation. *Advances in Neural Information Processing Systems*, 37:134614–134644, 2024.

Alcaraz, J. M. L. and Strodthoff, N. Diffusion-based time series imputation and forecasting with structured state space models. *arXiv preprint arXiv:2208.09399*, 2022.

Austin, J., Johnson, D. D., Ho, J., Tarlow, D., and Van Den Berg, R. Structured denoising diffusion models in discrete state-spaces. *Advances in neural information processing systems*, 34:17981–17993, 2021.

Baldan, G., Liu, Q., Guardone, A., and Thurey, N. Flow matching meets pdes: A unified framework for physics-constrained generation. *arXiv preprint arXiv:2506.08604*, 2025.

Bastek, J.-H., Sun, W., and Kochmann, D. M. Physics-informed diffusion models. *arXiv preprint arXiv:2403.14404*, 2024.

Blau, T., Ganz, R., Kawar, B., Bronstein, A., and Elad, M. Threat model-agnostic adversarial defense using diffusion models. *arXiv preprint arXiv:2207.08089*, 2022.

Chen, S., Sun, P., Song, Y., and Luo, P. Diffusiondet: Diffusion model for object detection. In *Proceedings of the IEEE/CVF international conference on computer vision*, pp. 19830–19843, 2023.

Cheng, S. and Alkhalifah, T. Diffpinn: Generative diffusion-initialized physics-informed neural networks for accelerating seismic wavefield representation. *arXiv preprint arXiv:2506.00471*, 2025.

Chi, C., Xu, Z., Feng, S., Cousineau, E., Du, Y., Burchfiel, B., Tedrake, R., and Song, S. Diffusion policy: Visuomotor policy learning via action diffusion. *The International Journal of Robotics Research*, pp. 02783649241273668, 2023.

Croitoru, F.-A., Hondru, V., Ionescu, R. T., and Shah, M. Diffusion models in vision: A survey. *IEEE transactions on pattern analysis and machine intelligence*, 45(9):10850–10869, 2023.

Dhariwal, P. and Nichol, A. Diffusion models beat gans on image synthesis. *Advances in neural information processing systems*, 34:8780–8794, 2021.

Efron, B. Bayes’ theorem in the 21st century. *Science*, 340 (6137):1177–1178, 2013.

Fitzpatrick, R. *Plasma physics: an introduction*. Crc Press, 2022.

Fu, W., Zhou, R., Gao, Y., Guo, Z., and Yu, Q. A diffusion model-based deep learning approach for denoising acoustic emission signals in concrete. *Measurement*, 251:117143, 2025.

Gao, X., Sitharam, M., and Roitberg, A. E. Bounds on the jensen gap, and implications for mean-concentrated distributions. *arXiv preprint arXiv:1712.05267*, 2017.

Ghanem, P., Demirkaya, A., Imbiriba, T., Ramezani, A., Danziger, Z., and Erdogmus, D. Learning physics informed neural odes with partial measurements. In Hansen, N. (ed.), *Proceedings of the 41st International Conference on Machine Learning*, pp. 1234–1245, Vienna, Austria, 2024. PMLR.

Greenwald, M., Bader, A., Baek, S., Bakhtiari, M., Barnard, H., Beck, W., Bergerson, W., Bespamyatnov, I., Bonoli, P., Brower, D., et al. 20 years of research on the alcator c-mod tokamak. *Physics of Plasmas*, 21(11), 2014.

Hang, T., Gu, S., Li, C., Bao, J., Chen, D., Hu, H., Geng, X., and Guo, B. Efficient diffusion training via min-snr weighting strategy. In *Proceedings of the IEEE/CVF international conference on computer vision*, pp. 7441–7451, 2023.

He, K., Zhang, X., Ren, S., and Sun, J. Deep residual learning for image recognition. In *Proceedings of the IEEE conference on computer vision and pattern recognition*, pp. 770–778, 2016.

Ho, J., Jain, A., and Abbeel, P. Denoising diffusion probabilistic models. *Advances in neural information processing systems*, 33:6840–6851, 2020.

Huang, J., Yang, G., Wang, Z., and Park, J. J. Diffusion-pde: Generative pde-solving under partial observation. *Advances in Neural Information Processing Systems*, 37: 130291–130323, 2024.

Hubbert, M. K. Darcy’s law and the field equations of the flow of underground fluids. *Transactions of the AIME*, 207(01):222–239, 1956.

Ip, A., Irio, L., and Oliveira, R. Vehicle trajectory prediction based on lstm recurrent neural networks. In *2021 IEEE 93rd vehicular technology conference (VTC2021-Spring)*, pp. 1–5. IEEE, 2021.

Ito, K. and Xiong, K. Gaussian filters for nonlinear filtering problems. *IEEE transactions on automatic control*, 45 (5):910–927, 2002.

Jacobsen, C., Zhuang, Y., and Duraisamy, K. Cocogen: Physically consistent and conditioned score-based generative models for forward and inverse problems. *SIAM Journal on Scientific Computing*, 47(2):C399–C425, 2025.

Karras, T., Aittala, M., Aila, T., and Laine, S. Elucidating the design space of diffusion-based generative models. *Advances in neural information processing systems*, 35: 26565–26577, 2022.

Kotz, S., Kozubowski, T., and Podgorski, K. *The Laplace distribution and generalizations: a revisit with applications to communications, economics, engineering, and finance*. Springer Science & Business Media, 2012.

LaBombard, B., Hughes, J., Mossessian, D., Greenwald, M., Lipschultz, B., Terry, J., Team, A. C.-M., et al. Evidence for electromagnetic fluid drift turbulence controlling the edge plasma state in the alcator c-mod tokamak. *Nuclear fusion*, 45(12):1658, 2005.

Lee, S., Jo, J., and Hwang, S. J. Exploring chemical space with score-based out-of-distribution generation. In *International Conference on Machine Learning*, pp. 18872–18892. PMLR, 2023.

Li, H., Ditzler, G., Roveda, J., and Li, A. Descod-ecg: Deep score-based diffusion model for ecg baseline wander and noise removal. *IEEE Journal of Biomedical and Health Informatics*, 28(9):5081–5091, 2023.

Li, X., Ren, Y., Jin, X., Lan, C., Wang, X., Zeng, W., Wang, X., and Chen, Z. Diffusion models for image restoration and enhancement: a comprehensive survey. *International Journal of Computer Vision*, 133(11):8078–8108, 2025.

Li, Z., Kovachki, N., Azizzadenesheli, K., Liu, B., Bhattacharya, K., Stuart, A., and Anandkumar, A. Fourier neural operator for parametric partial differential equations. *arXiv preprint arXiv:2010.08895*, 2020.

Liu, J., Wang, Q., Fan, H., Wang, Y., Tang, Y., and Qu, L. Residual denoising diffusion models. In *Proceedings of the IEEE/CVF Conference on Computer Vision and Pattern Recognition*, pp. 2773–2783, 2024.

Long, J., Shelhamer, E., and Darrell, T. Fully convolutional networks for semantic segmentation. In *Proceedings of the IEEE conference on computer vision and pattern recognition*, pp. 3431–3440, 2015.

Long, K., Shi, X., and Li, X. Physics-informed neural network for cross-dynamics vehicle trajectory stitching. *Transportation Research Part B: Methodological*, 2022.

Lu, L., Jin, P., and Karniadakis, G. E. Deeponet: Learning nonlinear operators for identifying differential equations based on the universal approximation theorem of operators. *arXiv preprint arXiv:1910.03193*, 2019.

Luo, S., Su, Y., Peng, X., Wang, S., Peng, J., and Ma, J. Antigen-specific antibody design and optimization with diffusion-based generative models for protein structures. *Advances in Neural Information Processing Systems*, 35: 9754–9767, 2022.

Mathews, A., Francisquez, M., Hughes, J. W., Hatch, D. R., Zhu, B., and Rogers, B. N. Uncovering turbulent plasma dynamics via deep learning from partial observations. *Physical Review E*, 104(2):025205, 2021.

Mitchell, W. C., Staniforth, A., and Scott, I. Analysis of ackermann steering geometry. Technical report, SAE Technical Paper, 2006.

Pensoneault, A. and Zhu, X. Efficient bayesian physics informed neural networks for inverse problems via ensemble kalman inversion. *Journal of Computational Physics*, 508:113006, 2024.

Perez, E., Strub, F., De Vries, H., Dumoulin, V., and Courville, A. Film: Visual reasoning with a general conditioning layer. In *Proceedings of the AAAI conference on artificial intelligence*, volume 32, 2018.

Qiu, J., Huang, J., Zhang, X., Lin, Z., Pan, M., Liu, Z., and Miao, F. Pi-fusion: Physics-informed diffusion model for learning fluid dynamics. *arXiv preprint arXiv:2406.03711*, 2024.

Raissi, M., Perdikaris, P., and Karniadakis, G. Physics-informed neural networks: A deep learning framework for solving forward and inverse problems involving nonlinear partial differential equations. *Journal of Computational Physics*, 378:686–707, 2019.

Ribeiro, M. I. Kalman and extended kalman filters: Concept, derivation and properties. *Institute for Systems and Robotics*, 43(46):3736–3741, 2004.

Rixner, M. and Koutsourelakis, P.-S. A probabilistic generative model for semi-supervised training of coarse-grained surrogates and enforcing physical constraints through virtual observables. *Journal of Computational Physics*, 434:110218, 2021.

Sanokowski, S., Hochreiter, S., and Lehner, S. A diffusion model framework for unsupervised neural combinatorial optimization. *arXiv preprint arXiv:2406.01661*, 2024.

Shan, S., Zhu, M., Lin, Y., and Lu, L. Red-diffeq: Regularization by denoising diffusion models for solving inverse pde problems with application to full waveform inversion. *arXiv preprint arXiv:2509.21659*, 2025.

Shi, Z., Yu, L., Xie, T., and Zhang, C. Diffusion-pinn sampler. *arXiv preprint arXiv:2410.15336*, 2024.

Shu, D., Li, Z., and Farimani, A. B. A physics-informed diffusion model for high-fidelity flow field reconstruction. *Journal of Computational Physics*, 478:111972, 2023.

Song, J., Meng, C., and Ermon, S. Denoising diffusion implicit models. *arXiv preprint arXiv:2010.02502*, 2020a.

Song, Y., Sohl-Dickstein, J., Kingma, D. P., Kumar, A., Ermon, S., and Poole, B. Score-based generative modeling through stochastic differential equations. *arXiv preprint arXiv:2011.13456*, 2020b.

Soni, J., Lange-Hegermann, M., and Windmann, S. Physics-informed diffusion models for unsupervised anomaly detection in multivariate time series. *arXiv preprint arXiv:2508.11528*, 2025.

Tee, J. T. J., Zhang, K., Yoon, H. S., Gowda, D. N., Kim, C., and Yoo, C. D. Physics informed distillation for diffusion models. *arXiv preprint arXiv:2411.08378*, 2024.

Wang, S., Dou, Z., Shan, S., Liu, T.-R., and Lu, L. Fundiff: Diffusion models over function spaces for physics-informed generative modeling. *arXiv preprint arXiv:2506.07902*, 2025a.

Wang, Y., Liu, Q., Jiang, Z., Wang, T., Jiao, J., Chu, H., Gao, B., and Chen, H. Rad: Retrieval-augmented decision-making of meta-actions with vision-language models in autonomous driving. In *Proceedings of the Computer Vision and Pattern Recognition Conference*, pp. 3838–3848, 2025b.

Yang, L., Zhang, Z., Song, Y., Hong, S., Xu, R., Zhao, Y., Zhang, W., Cui, B., and Yang, M.-H. Diffusion models: A comprehensive survey of methods and applications. *ACM computing surveys*, 56(4):1–39, 2023.

Yang, W. and Zhang, X. Pis: A generalized physical inversion solver for arbitrary sparse observations via set-conditioned diffusion. *arXiv preprint arXiv:2512.13732*, 2025.

Yi, H., Hou, L., Jin, Y., Saeed, N. A., Kandil, A., and Duan, H. Time series diffusion method: A denoising diffusion probabilistic model for vibration signal generation. *Mechanical Systems and Signal Processing*, 216:111481, 2024.

Yoon, J., Hwang, S. J., and Lee, J. Adversarial purification with score-based generative models. In *International Conference on Machine Learning*, pp. 12062–12072. PMLR, 2021.

Zeng, T., Wang, T., Yu, L., Liu, Z., Chen, H., and Chen, X. Wheel load estimation and anti-roll bar control using suspension analysis with neural network. In *IFTOMM World Congress on Mechanism and Machine Science*, pp. 332–342. Springer, 2023.

Zeng, T., Liu, Z., He, C., Zeng, Z., Chen, H., Zhang, F., Fu, K., and Chen, X. Analysis and design of suspension state observer for wheel load estimation. In SAE (ed.), *SAE Technical Paper 2024-01-2285*, pp. 09 Apr 2024, Warrendale, PA, 2024. SAE International.

Zhang, Q. and Chen, Y. Fast sampling of diffusion models with exponential integrator. *arXiv preprint arXiv:2204.13902*, 2022.

Zhang, Y. and Zou, D. Physics-informed distillation of diffusion models for pde-constrained generation. *arXiv preprint arXiv:2505.22391*, 2025.

Zweben, S. J., Terry, J., Stotler, D., and Maqueda, R. J. Invited review article: Gas puff imaging diagnostics of edge plasma turbulence in magnetic fusion devices. *Review of Scientific Instruments*, 88(4), 2017.

A. Appendix A

A.1. Preliminary of Physics Informed Neural Networks

Typically, physical laws are expressed as a set of ODEs or PDEs. For brevity, ODEs are regarded herein as PDEs with only one independent variable, and no additional preliminary of PINNs on ODEs will be provided. The PDEs over a domain $\Omega \subset \mathbb{R}^d$ (Raissi et al., 2019) is expressed as:

$$\mathcal{D}[\mathbf{u}(\mathbf{x}), \mathbf{x}] = 0, \text{ for } \mathbf{x} = (x_1, x_2, \dots, x_d)^\top \in \Omega, \quad (21)$$

with boundary conditions:

$$\mathcal{B}[\mathbf{u}(\mathbf{x}), \mathbf{x}] = 0, \text{ for } \mathbf{x} \in \partial\Omega, \quad (22)$$

where \mathcal{D} is the differential operator and \mathcal{B} defines the boundary conditions, $\partial\Omega$ is the boundary of Ω , and \mathbf{u} is modeled as the solution field for all data $\mathbf{x} \in \Omega$ satisfying the PDEs' set and boundary constraints.

In PINNs, the solution $\mathbf{u}(\mathbf{x})$ is approximated by a deep neural network, denoted as $\hat{\mathbf{u}}(\mathbf{x}; \boldsymbol{\theta})$, where $\boldsymbol{\theta}$ represents the set of all learnable parameters.

The discrepancy between the results calculated by the neural network and by physical model is represented by a residual $\mathcal{R}(\mathbf{x}; \boldsymbol{\theta})$, which is defined by:

$$\mathcal{R}(\mathbf{x}; \boldsymbol{\theta}) := \mathcal{D}[\hat{\mathbf{u}}(\mathbf{x}; \boldsymbol{\theta}), \mathbf{x}], \quad (23)$$

which also satisfies the boundary $\mathcal{B}[\hat{\mathbf{u}}(\mathbf{x}; \boldsymbol{\theta}), \mathbf{x}] = 0$.

The parameters $\boldsymbol{\theta}$ are optimized by minimizing a physical loss $\mathcal{L}_p(\boldsymbol{\theta})$, which typically includes a term for the PDE residual and another term for the boundary deviation penalty:

$$\mathcal{L}_p(\boldsymbol{\theta}) = \frac{1}{N_f} \sum_{i=1}^{N_f} \|\mathcal{R}(\mathbf{x}_f^i; \boldsymbol{\theta})\|_2^2 + \frac{1}{N_b} \sum_{i=1}^{N_b} \|\mathcal{B}[\hat{\mathbf{u}}(\mathbf{x}_b^i; \boldsymbol{\theta}), \mathbf{x}_b^i]\|_2^2, \quad (24)$$

where $\{\mathbf{x}_f^i\}_{i=1}^{N_f}$ is a set of N_f collocation points sampled from the domain Ω , where the PDE residual is enforced, and $\{\mathbf{x}_b^i\}_{i=1}^{N_b}$ is a set of N_b points sampled from the boundary $\partial\Omega$, where the boundary conditions are enforced.

A Data-driven loss $\mathcal{L}_d(\boldsymbol{\theta})$ is presented as:

$$\mathcal{L}_d(\boldsymbol{\theta}) = \frac{1}{N_d} \sum_{i=1}^{N_d} \|\hat{\mathbf{u}}(\mathbf{x}_d^i; \boldsymbol{\theta}) - \mathbf{u}^i\|_2^2, \quad (25)$$

where \mathbf{u}^i here is the data ground truth. Total loss $\mathcal{L}(\boldsymbol{\theta})$ becomes weighted sum of $\mathcal{L}_p(\boldsymbol{\theta})$ and $\mathcal{L}_d(\boldsymbol{\theta})$.

A.2. Consistency

To theoretically validate the consistency of the proposed PILD framework, we analyze the model from the perspective of score-based generative modeling (Song et al., 2020b), extending the continuous-time diffusion formulation to incorporate physical constraints. This section demonstrates that integrating the physics-informed residual term into the training objective does not compromise the model's ability to recover the true data distribution $q(\mathbf{x}_0)$.

A.2.1. CONTINUOUS-TIME DIFFUSION FORMULATION

We first formalize the forward diffusion process as a stochastic differential equation (SDE) over a continuous time interval $t \in [0, T]$:

$$d\mathbf{x}_t = \mathbf{F}_t \mathbf{x}_t dt + \mathbf{G}_t d\mathbf{w}_t, \quad (26)$$

where \mathbf{w}_t denotes a standard Wiener process, $\mathbf{F}_t \in \mathbb{R}^{D \times D}$ is the drift coefficient, and $\mathbf{G}_t \in \mathbb{R}^{D \times D}$ is the diffusion coefficient. For consistency with the discrete diffusion setup in the main text, we adopt the parameterization aligned with DDPM (Ho et al., 2020):

$$\mathbf{F}_t = \frac{1}{2} \frac{d \log \bar{\alpha}_t}{dt} \mathbf{I}, \quad \mathbf{G}_t = \sqrt{-\frac{d \log \bar{\alpha}_t}{dt}} \mathbf{I}, \quad (27)$$

where $\bar{\alpha}_t = \prod_{i=1}^t \alpha_i$ (extended to continuous time) decreases from $\bar{\alpha}_0 \approx 1$ to $\bar{\alpha}_T \approx 0$.

The reverse diffusion process, which generates samples by inverting the forward SDE, follows the parameterization (Zhang & Chen, 2022):

$$d\mathbf{x}_t = \left[F_t \mathbf{x}_t - \frac{1 + \lambda^2}{2} \mathbf{G}_t \mathbf{G}_t^\top \nabla_{\mathbf{x}_t} \log p_t(\mathbf{x}_t) \right] d\bar{t} + \lambda \mathbf{G}_t d\bar{w}_t, \quad (28)$$

where $\bar{t} = T - t$ is the reversed time, \bar{w}_t is a reversed Wiener process, and $\lambda \geq 0$ controls the stochasticity ($\lambda = 1$ for DDPM, $\lambda = 0$ for deterministic DDIM). The score function $\nabla_{\mathbf{x}_t} \log p_t(\mathbf{x}_t)$ quantifies the log-density gradient of the noisy data distribution at time t .

A.2.2. PHYSICS-INFORMED SCORE MATCHING OBJECTIVE

The core of PILD’s consistency lies in unifying data-driven score matching with physical constraint enforcement. We define the extended score-matching objective as:

$$\mathbf{s}_{\text{opt}} = \arg \min_{\mathbf{s}} \mathbb{E}_{t \sim \text{Unif}[0, T]} \mathbb{E}_{q(\mathbf{x}_0)q(\mathbf{x}_t|\mathbf{x}_0)} \left[\Lambda(t) \|\nabla_{\mathbf{x}_t} \log q(\mathbf{x}_t|\mathbf{x}_0) - \mathbf{s}(\mathbf{x}_t, t, \mathbf{O})\|_2^2 - \log q_{\mathcal{R}}(\hat{\mathbf{r}} = \mathbf{0}|\mathbf{x}_0^*(\mathbf{x}_t, t, \mathbf{O})) \right], \quad (29)$$

where $\Lambda(t) > 0$ is a time-dependent weighting factor (consistent with Min-SNR weighting (Hang et al., 2023)), $\mathbf{s}(\mathbf{x}_t, t, \mathbf{O})$ is the parameterized score function (incorporating physical observer \mathbf{O} via conditional embedding), $\mathbf{x}_0^* = \text{DDIM}[\mathbf{x}_t, \mathbf{O}, t]$ is the denoised estimate of \mathbf{x}_0 from PILD’s sampling process, $q_{\mathcal{R}}(\hat{\mathbf{r}}|\mathbf{x}_0^*) = \text{Laplace}(\hat{\mathbf{r}}; \mathcal{R}(\mathbf{x}_0^*), b_t \mathbf{I})$ is the Laplace-distributed virtual residual likelihood.

The Jensen gap $\mathcal{R}(\mathbb{E}[\mathbf{x}_0|\mathbf{x}_t]) \neq \mathbb{E}[\mathcal{R}(\mathbf{x}_0)|\mathbf{x}_t]$ arises because the residual operator \mathcal{R} (e.g., PDE differential operator) is non-linear, making the expectation and residual operator non-commutable. For mean estimation ($\hat{\mathbf{x}}_0 = \mathbb{E}[\mathbf{x}_0|\mathbf{x}_t]$), this gap introduces a systematic bias in the physical loss, as $\mathcal{R}(\hat{\mathbf{x}}_0)$ cannot accurately approximate $\mathbb{E}[\mathcal{R}(\mathbf{x}_0)|\mathbf{x}_t]$. In contrast, $\mathbf{x}_0^* = \text{DDIM}[\mathbf{x}_t, \mathbf{O}, t]$ is a sample from $p(\mathbf{x}_0|\mathbf{x}_t, \mathbf{O})$, so the law of large numbers ensures that $\mathbb{E}_{\mathbf{x}_0^* \sim p(\mathbf{x}_0|\mathbf{x}_t, \mathbf{O})}[\mathcal{R}(\mathbf{x}_0^*)] = \mathbb{E}[\mathcal{R}(\mathbf{x}_0)|\mathbf{x}_t]$ (when DDIM sampling is accurate). This directly reduces the Jensen gap in expectation (Bastek et al., 2024), as the physical loss is now computed over samples of \mathbf{x}_0 rather than its mean.

We now establish the consistency of the extended objective with the following proposition:

Proposition A.1. *Let $q(\mathbf{x}_0)$ be a data distribution whose samples satisfy the physical constraint $\mathcal{R}(\mathbf{x}_0) = \mathbf{0}$. If the optimal score \mathbf{s}_{opt} minimizes the extended objective in Equation (29), then solving the reverse SDE (28) with \mathbf{s}_{opt} generates samples from the true distribution $\mathbf{x}_0 \sim q(\mathbf{x}_0)$.*

Proof. For standard diffusion models, perfect score recovery $\mathbf{s}(\mathbf{x}_t, t) = \nabla_{\mathbf{x}_t} \log p_t(\mathbf{x}_t)$ ensures that the reverse SDE’s marginal distribution $p^*(\mathbf{x}_t)$ matches the forward diffusion distribution $q(\mathbf{x}_t)$ for all t (Zhang & Chen, 2022). Sampling from $p(\mathbf{x}_T) \sim \mathcal{N}(\mathbf{0}, \mathbf{I})$ and solving the reverse SDE thus recovers $\mathbf{x}_0 \sim q(\mathbf{x}_0)$.

For the physics-informed term, substituting $q_{\mathcal{R}}(\hat{\mathbf{r}}|\mathbf{x}_0^*)$ into the objective yields:

$$-\log q_{\mathcal{R}}(\hat{\mathbf{r}} = \mathbf{0}|\mathbf{x}_0^*) = \frac{1}{b_t} \|\mathcal{R}(\mathbf{x}_0^*)\|_1 + C, \quad (30)$$

where C is a constant independent of \mathbf{x}_0^* and \mathbf{s} . Since $\mathbf{x}_0 \sim q(\mathbf{x}_0)$ satisfies $\mathcal{R}(\mathbf{x}_0) = \mathbf{0}$, the denoised estimate $\mathbf{x}_0^* \rightarrow \mathbf{x}_0$ as $t \rightarrow 0$ (by diffusion model convergence). Thus, the optimal score \mathbf{s}_{opt} that minimizes the data-driven score matching term also minimizes the physical residual term.

The extended objective combines two compatible terms: the data-driven term ensures alignment with $q(\mathbf{x}_0)$, and the physics-informed term enforces $\mathcal{R}(\mathbf{x}_0) = \mathbf{0}$. Since these terms do not conflict (physical constraints are inherent to $q(\mathbf{x}_0)$), \mathbf{s}_{opt} recovers the true score function. Solving the reverse SDE with \mathbf{s}_{opt} therefore generates samples from $q(\mathbf{x}_0)$ that satisfy the physical constraints. \square

A.2.3. PRACTICAL IMPLICATIONS

The proposition confirms that PILD’s integration of physical constraints via Laplace-distributed virtual residuals and conditional embedding preserves the diffusion model’s core consistency. Key practical insights include: Discretization of the

continuous SDE (e.g., DDIM sampling) introduces negligible bias that diminishes with sufficient diffusion steps T (Song et al., 2020a). The conditional embedding module (U-FiLM/U-Att) encodes \mathcal{O} into the score function without breaking distribution recovery. The gate function $G(t)$ and time-dependent variance b_t adaptively balance constraint enforcement across noise levels, ensuring stability without compromising consistency.

The rationale for virtual residual modeling with the Laplace distribution and the design of the gating function will be presented in the next two subsections.

A.3. Laplace Distribution

In our framework, the virtual residual observation, which is defined as the discrepancy between the generated sample and the physical constraint, is modeled using a Laplace distribution. This choice is theoretically and practically well-motivated for several reasons.

First, compared to the Gaussian distribution, the Laplace distribution exhibits heavier tails, which makes it significantly more robust to outliers and large deviations. Specifically, the probability density function (PDF) of a univariate Laplace distribution centered at zero is given by:

$$p(r|b) = \frac{1}{2b} \exp\left(-\frac{|r|}{b}\right), \quad (31)$$

where r denotes the residual and $b > 0$ is the scale parameter. In contrast, the Gaussian PDF decays quadratically in the exponent ($\exp(-r^2/2\sigma^2)$), causing it to assign exponentially smaller probabilities to large residuals. The Laplace distribution, owing to its heavier tails, is better suited to model the residuals arising from real-world complex systems that often exhibit outliers and non-Gaussian noise, thereby leading to improved performance in practice.

Second, from an optimization perspective, adopting a Laplace distribution on the virtual residual corresponds to minimizing the ℓ_1 -norm of the physical violation during training. This is because maximizing the log-likelihood of the Laplace model is equivalent to solving:

$$\min_{\theta} \mathbb{E}_{x \sim p_{\theta}} [\|\mathcal{L}(x)\|_1], \quad (32)$$

where $\mathcal{L}(x)$ denotes the residual of the physical operator (e.g., PDE residual) evaluated on the generated sample x , and θ represents the parameters of the diffusion model. The ℓ_1 penalty is known to promote sparsity and robustness, which aligns with our goal of enforcing physical laws while tolerating noise or outliers. Moreover, under mild regularity conditions on the underlying PDE/ODE operator, this formulation ensures convergence of the training objective to a physically plausible solution, as the expected residual vanishes when the generated distribution aligns with the manifold defined by the physical constraints.

Third, the Laplace assumption facilitates theoretical analysis of the posterior consistency in our physics-informed diffusion framework. Because the Laplace likelihood is log-concave and its score function (i.e., derivative of log-density) is piecewise constant ($\nabla_r \log p(r) = -\text{sign}(r)/b$), it leads to well-behaved gradient dynamics during reverse diffusion. This contrasts with heavy-tailed alternatives (e.g., Cauchy) that may cause unstable training, or light-tailed distributions (e.g., Gaussian) that over-penalize moderate residuals. Empirically, we observe faster convergence and improved generalization when using Laplace-distributed virtual observations, particularly in high-dimensional or stiff dynamical systems.

In summary, the Laplace distribution provides an optimal trade-off between fidelity to physical laws and robustness to real-world imperfections, making it particularly suitable for modeling virtual residual observations.

A.4. Gating Function

Since $G(t)$ is strictly positive for all valid inputs, the minimization of the total loss $\mathcal{L}_{\text{PILD}}$ still necessitates driving the physical residual $\|\mathcal{R}(\hat{x}_0)\|_1$ towards zero. Therefore, the global minimum of $\mathcal{L}_{\text{PILD}}$ still corresponds to a model ϵ_{θ} that optimally learns the score function of a distribution $q^*(\mathbf{x}_0|\mathcal{O})$. This $q^*(\mathbf{x}_0|\mathcal{O})$ is characterized by samples \hat{x}_0 that are, in expectation, statistically indistinguishable from the true data $q(\mathbf{x}_0)$ and simultaneously robustly adhere to the physical constraints $\mathcal{R}(\mathbf{x}_0) = 0$, with the adherence adaptively emphasized based on the model's confidence. This synergistic robust and adaptively weighted probabilistic optimization ensures that the learned distribution is a resilient, physically-grounded generative model of the underlying system. Additionally, our gating function $G(t)$ introduces a time-step-aware modulation mechanism that is decoupled from the data's variance characteristics. By anchoring the scheduling logic to the denoising timestep t , we ensure robust and predictable guidance for physical constraint enforcement, independent of training dynamics.

A.5. Unified Training Objective

The original optimization objective involves sampling latent trajectories from the learned distribution $\mathbf{x}_{1:T} \sim p_\theta(\mathbf{x}_{1:T})$. To make this computationally tractable, we instead sample from the known forward process $q(\mathbf{x}_{1:T})$. This approximation effectively disregards the likelihood ratio term, which simplifies the objective while introducing a small bias. We argue that this bias diminishes during training, as optimizing the variational lower bound encourages $p_\theta(\mathbf{x}_{1:T})$ to converge toward $q(\mathbf{x}_{1:T})$, which is proven by:

$$\begin{aligned}
 & \mathbb{E}_{\mathbf{x}_0 \sim q(\mathbf{x}_0)} [-\log p_\theta(\mathbf{x}_0)] + \mathbb{E}_{\mathbf{x}_{1:T} \sim p_\theta(\mathbf{x}_{1:T})} [-\log q_{\mathcal{R}}(\hat{\mathbf{r}} = \mathbf{0} | \mathbf{x}_0^*(\mathbf{x}_{1:T}))] \\
 & \leq \mathbb{E}_{q(\mathbf{x}_{0:T})} \left[\log \frac{q(\mathbf{x}_{1:T} | \mathbf{x}_0)}{p_\theta(\mathbf{x}_{0:T})} \right] + \mathbb{E}_{\mathbf{x}_{1:T} \sim p_\theta(\mathbf{x}_{1:T})} [-\log q_{\mathcal{R}}(\hat{\mathbf{r}} = \mathbf{0} | \mathbf{x}_0^*(\mathbf{x}_{1:T}))] \\
 & = \mathbb{E}_{q(\mathbf{x}_{0:T})} \left[\log \frac{q(\mathbf{x}_{1:T} | \mathbf{x}_0)}{p_\theta(\mathbf{x}_{0:T})} \right] + \mathbb{E}_{\mathbf{x}_{1:T} \sim q(\mathbf{x}_{1:T})} \left[-\frac{p_\theta(\mathbf{x}_{1:T})}{q(\mathbf{x}_{1:T})} \log q_{\mathcal{R}}(\hat{\mathbf{r}} = \mathbf{0} | \mathbf{x}_0^*(\mathbf{x}_{1:T})) \right] \\
 & \approx \mathbb{E}_{q(\mathbf{x}_{0:T})} \left[\log \frac{q(\mathbf{x}_{1:T} | \mathbf{x}_0)}{p_\theta(\mathbf{x}_{0:T})} \right] + \mathbb{E}_{\mathbf{x}_{1:T} \sim q(\mathbf{x}_{1:T})} [-\log q_{\mathcal{R}}(\hat{\mathbf{r}} = \mathbf{0} | \mathbf{x}_0^*(\mathbf{x}_{1:T}))] \\
 & = \mathbb{E}_{q(\mathbf{x}_{0:T})} \left[\log \frac{q(\mathbf{x}_{1:T} | \mathbf{x}_0)}{p_\theta(\mathbf{x}_{0:T})} - \log q_{\mathcal{R}}(\hat{\mathbf{r}} = \mathbf{0} | \mathbf{x}_0^*(\mathbf{x}_{1:T})) \right].
 \end{aligned} \tag{33}$$

Building on the unified objective in Equation (33), we further derive the final loss $\mathcal{L}_{\text{PILD}}(\boldsymbol{\theta})$ with key steps as follows:

Data Loss Term ($\lambda_t \|\epsilon - \epsilon_\theta\|^2$). The data-driven component originates from the variational lower bound of diffusion models. As shown in Equation (8), the core training objective of denoising diffusion models is to minimize the MSE between the true noise ϵ and the model-predicted noise $\epsilon_\theta(x_t, O, t)$. The time-dependent weight λ_t (Min-SNR weighting) is introduced to balance the denoising loss across different noise levels t , which naturally arises from maximizing the data log-likelihood in score-based generative modeling.

Physics Loss Term ($\frac{1}{b_t} G(t) \|\mathcal{R}(x_0^*)\|_1$). The physics-informed component is derived from the Laplace-distributed virtual residual likelihood $q_{\mathcal{R}}(\hat{\mathbf{r}} = \mathbf{0} | \mathbf{x}_0^*)$ in Equation (14). Maximizing the log-likelihood of this virtual observation is equivalent to minimizing the ℓ_1 -norm of the physical residual $\mathcal{R}(x_0^*)$ (since $\log q_{\mathcal{R}}(\hat{\mathbf{r}} = \mathbf{0} | \mathbf{x}_0^*) \propto -\frac{1}{b_t} \|\mathcal{R}(x_0^*)\|_1$). The time-dependent variance $b_t = B_t/c$ modulates the strength of the physical penalty, while the gate function $G(t)$ amplifies the penalty for physical violations as t decreases (i.e., when the model approaches the clean data x_0). This term enforces the generated samples to satisfy the physical constraints $\mathcal{R}(x_0) = 0$.

By unifying these two components under the same expectation over $t \sim [1, T]$, $x_0 \sim q(x_0)$, O , and $\epsilon \sim \mathcal{N}(0, I)$, we obtain the final loss $\mathcal{L}_{\text{PILD}}(\boldsymbol{\theta})$ in Equation (15), which seamlessly integrates data-driven learning and physics-informed constraints.

A.6. Details of Implementation

The model training is conducted on an RTX 4090/24GB GPU. The setup of each experiment differs slightly, and the detailed configurations are provided in Tables 5 to 8.

Table 5. Implementation details of tracking task.

Hyperparameter	Value
U-Net latent dimensions	64 \rightarrow 128 \rightarrow 256
Attention heads of U-Att	-
MLP latent dimensions of U-FiLM	64
Time embedding dimension	128
Diffusion timesteps	100
Batch size	8
Iterations	10^4
Initial learning rate	10^{-3}
Optimization algorithm	Adam (Adam et al., 2014)
Physical penalty weight c	0.005
β_t -scheduler	Cosine schedule (Dhariwal & Nichol, 2021)
β_1, β_t	$10^{-4}, 0.03$

Table 6. Implementation details of tire force estimation.

Hyperparameter	Value
U-Net latent dimensions	128 → 192 → 256 → 320 → 384
Attention heads of U-Att	—
MLP latent dimensions of U-FiLM	96
Time embedding dimension	128
Diffusion timesteps	100
Batch size	32
Iterations	5×10^5
Initial learning rate	10^{-5}
Optimization algorithm	Adam (Adam et al., 2014)
Physical penalty weight c	0.0001
β_t -scheduler	Cosine schedule (Dhariwal & Nichol, 2021)
β_1, β_t	$10^{-4}, 0.03$

Table 7. Implementation details of Darcy flow.

Hyperparameter	Value
U-Net latent dimensions	32 → 64 → 128 → 256
Attention heads of U-Att	—
MLP latent dimensions of U-FiLM	—
Time embedding dimension	128
Diffusion timesteps	100
Batch size	8
Iterations	3×10^5
Initial learning rate	10^{-4}
Optimization algorithm	Adam (Adam et al., 2014)
Physical penalty weight c	0.001
β_t -scheduler	Cosine schedule (Dhariwal & Nichol, 2021)
β_1, β_t	$10^{-6}, 10^{-2}$

Table 8. Implementation details of plasma dynamics.

Hyperparameter	Value
U-Net latent dimensions	128 → 256 → 512 → 1024
Attention heads of U-Att	16
MLP latent dimensions of U-FiLM	—
Time embedding dimension	128
Diffusion timesteps	100
Batch size	32
Iterations	5×10^5
Initial learning rate	10^{-5}
Optimization algorithm	Adam (Adam et al., 2014)
Physical penalty weight c	0.00001
β_t -scheduler	Cosine schedule (Dhariwal & Nichol, 2021)
β_1, β_t	$10^{-6}, 10^{-2}$

It should be noted that due to the more complex physical properties of plasma, we adopt the U-Att conditional embedding method, while in the other two engineering scenarios, the U-FiLM conditional embedding is sufficient to achieve satisfactory results. The Darcy scenario is an unconditional generation task, so no embedding is applied.

A.7. Other Formations of Constraints

The proposed PILD framework is not limited to PDEs/ODEs but also naturally extends to algebraic equations and inequality constraints, which are prevalent in engineering design, optimization, and scientific computing. Hence, we detail the

integration of these constraint types into the PILD training objective, following a first-principles derivation consistent with the core framework. Furthermore, we present a toy experiment under the scenario of inequality constraints to better demonstrate the effectiveness of the proposed method.

A.7.1. ALGEBRAIC EQUATION CONSTRAINTS

Algebraic equations describe relationships between variables without involving derivatives, e.g., equilibrium conditions in structural design, material property constraints, or algebraic identities in physical systems. Consider an algebraic constraint of the form:

$$\mathcal{A}(x_0) = a_{\text{target}}, \quad x_0 \sim p_{\theta}(x_0|O), \quad (34)$$

where $\mathcal{A} : \mathbb{R}^D \rightarrow \mathbb{R}^k$ denotes the algebraic operator, $a_{\text{target}} \in \mathbb{R}^k$ is the target value (often 0 for equality constraints), and x_0 is the generated sample from PILD. To enforce this constraint, we first define the algebraic residual as:

$$\mathcal{R}_{\text{alg}}(x_0^*) = \mathcal{A}(x_0^*) - a_{\text{target}}, \quad (35)$$

where $x_0^* = \text{DDIM}[x_t, O, t]$ is the denoised estimate of x_0 . Following PILD's probabilistic modeling paradigm, we treat $\mathcal{R}_{\text{alg}}(x_0^*)$ as a virtual residual observation $\hat{r}_{\text{alg}} = 0$ sampled from a Laplace distribution:

$$q_{\mathcal{R}_{\text{alg}}}(\hat{r}_{\text{alg}}|x_0^*) = \text{Laplace}(\hat{r}_{\text{alg}}; \mathcal{R}_{\text{alg}}(x_0^*), b_t I). \quad (36)$$

Then integrating this into PILD's total loss, the extended loss becomes:

$$\mathcal{L}_{\text{PILD-alg}}(\theta) = \mathbb{E}_{t \sim [1, T], x_0 \sim q(x_0), O, \epsilon \sim \mathcal{N}(0, I)} \left[\lambda_t \|\epsilon - \epsilon_{\theta}\|^2 + \frac{1}{b_t} G(t) \|\mathcal{R}_{\text{alg}}(x_0^*)\|_1 \right], \quad (37)$$

which is the same formation as the loss of PDEs/ODEs.

A.7.2. INEQUALITY CONSTRAINTS

Inequality constraints are ubiquitous in practical problems. Consider a general inequality constraint:

$$\mathcal{H}(x_0) \leq h_{\text{max}}, \quad x_0 \sim p_{\theta}(x_0|O), \quad (38)$$

where $\mathcal{H} : \mathbb{R}^D \rightarrow \mathbb{R}^m$ is the inequality operator, and $h_{\text{max}} \in \mathbb{R}^m$ is the upper bound. We transform the inequality into a residual via the ReLU function (Bastek et al., 2024), which activates only when the constraint is violated:

$$\mathcal{R}_{\text{ineq}}(x_0^*) = \text{ReLU}(\mathcal{H}(x_0^*) - h_{\text{max}}) = \max(0, \mathcal{H}(x_0^*) - h_{\text{max}}). \quad (39)$$

This residual is zero when the constraint is satisfied ($\mathcal{H}(x_0^*) \leq h_{\text{max}}$) and positive otherwise, effectively penalizing violations. We model $\mathcal{R}_{\text{ineq}}(x_0^*)$ as a Laplace-distributed virtual residual $\hat{r}_{\text{ineq}} = 0$:

$$q_{\mathcal{R}_{\text{ineq}}}(\hat{r}_{\text{ineq}}|x_0^*) = \text{Laplace}(\hat{r}_{\text{ineq}}; \mathcal{R}_{\text{ineq}}(x_0^*), b_t I). \quad (40)$$

For PILD's total loss, integrating the inequality constraint yields:

$$\mathcal{L}_{\text{PILD-ineq}}(\theta) = \mathbb{E}_{t \sim [1, T], x_0 \sim q(x_0), O, \epsilon \sim \mathcal{N}(0, I)} \left[\lambda_t \|\epsilon - \epsilon_{\theta}\|^2 + \frac{1}{b_t} G(t) \|\mathcal{R}_{\text{ineq}}(x_0^*)\|_1 \right], \quad (41)$$

which is also the same formation as PDEs/ODEs.

A.7.3. TOY EXPERIMENT

Since both equality constraints and inequality constraints can be transformed into similar forms, we only conduct the more complex experiment with inequality constraints here for brevity of presentation. This is a simple unconditional generation task, designed solely to demonstrate the effectiveness of the overall framework on other constraints. In this toy experiment, we establish four inequality constraints that form a parallelogram-shaped region. A total of 10000 training data points are

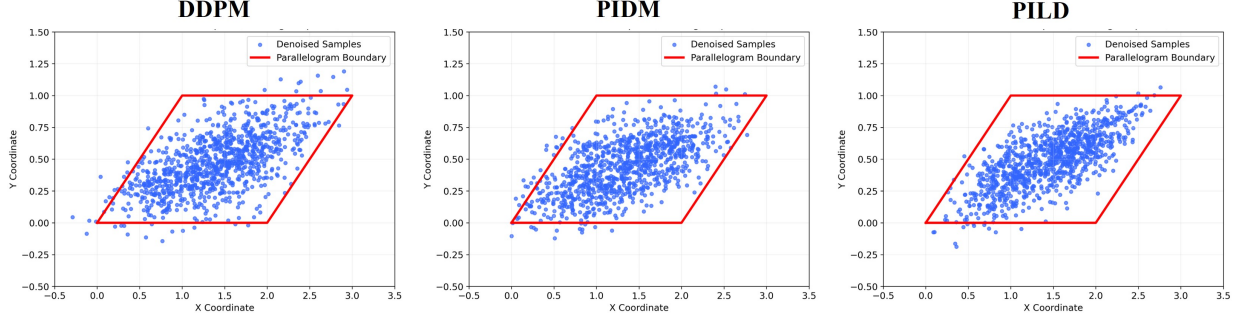


Figure 8. Results of toy experiment. The red parallelogram in the figure represents the constrained boundary, and the blue points denote the sampled data points.

randomly sampled from this region. Subsequently, the constraints specified in Equation (39) are applied to these inequalities to adapt them to the PILD architecture. The training is performed for 400 iterations. The results of DDPM, PIDM, and PILD are presented in Figure 8.

From the results, it can be observed that all three methods perform well on this simple task. However, DDPM, which only learns the data distribution, generates more outliers under such a data distribution with sharp boundaries. This is because the generation process of diffusion models may produce hallucinations at sharp boundaries (Aithal et al., 2024). In contrast, the two physics-informed methods yield superior sampling results. And PILD produces slightly fewer outliers than PIDM due to the better modeling of residual.

A.8. Details of Experimental Setup

A.8.1. VEHICLE TRACKING

When a vehicle is steering, the angles of the left and right wheels differ to enable both wheels to travel around the steering center simultaneously. This constitutes the most important feature of the Ackerman model, as illustrated in Figure 9. Furthermore, since the wheels are made of rubber, the lateral force during vehicle steering originates from the elastic force generated by rubber deformation. Consequently, there is an angle between the direction of the wheel's traveling speed and the geometric orientation of the wheel, which is known as the slip angle. The direction of the wheel's traveling speed is indicated by the red dashed line in Figure 9. In Figure 9, I is the vehicle's instantaneous center of steering; CG is the

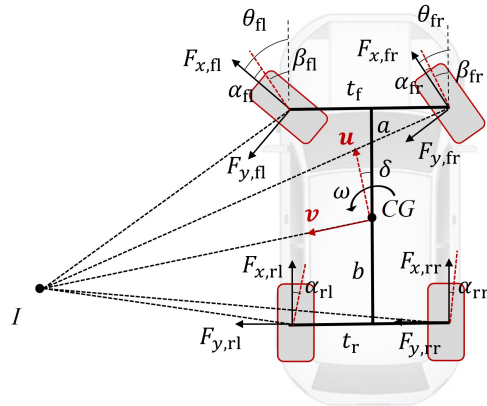


Figure 9. Ackerman model for tracking.

vehicle's center of mass; u , v , and ω are the longitudinal velocity, lateral velocity, and yaw rate at the vehicle's center of mass position, respectively, and the direction of the lateral velocity v points to the instantaneous center; the angle δ between

the longitudinal velocity u and the vehicle's longitudinal axis is the side slip angle of the center of mass. t_f , and t_r are the front and rear track widths, respectively; a and b are the distances from the center of mass to the front and rear axles.

Based on the above analysis, we can derive the following relationships:

$$m(\dot{u} - v\omega) = \sum F_u = F_{x,fr} \cos(\theta_{fr} + \delta) - F_{y,fr} \sin(\theta_{fr} + \delta) + F_{x,fl} \cos(\theta_{fl} + \delta) - F_{y,fl} \sin(\theta_{fl} + \delta) + (F_{x,rr} + F_{x,rl}) \cos \delta - (F_{y,rr} + F_{y,rl}) \sin \delta, \quad (42)$$

$$m(\dot{v} - u\omega) = \sum F_v = F_{x,fr} \sin(\theta_{fr} + \delta) + F_{y,fr} \cos(\theta_{fr} + \delta) + F_{x,fl} \sin(\theta_{fl} + \delta) + F_{y,fl} \cos(\theta_{fl} + \delta) + (F_{x,rr} + F_{x,rl}) \sin \delta + (F_{y,rr} + F_{y,rl}) \cos \delta, \quad (43)$$

$$I_z \dot{\omega} = \sum M_z = F_{x,fr} d_1 + F_{y,fr} d_2 - F_{x,fl} d_3 + F_{y,fl} d_4 + F_{x,rr} t_r/2 - F_{y,rr} b - F_{x,rl} t_r/2 - F_{y,rl} b = 0, \quad (44)$$

$$\theta_j = \alpha_j + \beta_j. \quad (45)$$

In Equations (42) to (45), F_u and F_v are the components of the adhesive force of each tire in the directions of the longitudinal velocity u and the lateral velocity v , respectively; M_z is the yaw moment of the adhesive force of each tire about the center of mass O ; m is the vehicle mass; I_z is the moment of inertia of the vehicle about the vertical axis passing through the center of mass; F_{xi} is the longitudinal adhesive force of the tire, $i = fr, fl, rr, rl$; F_{yi} is the lateral adhesive force of the tire; θ_j is the front wheel steering angle, $j = fr, fl$; α_i is the tire side slip angle; β_i is the angle between the tire velocity direction and the vehicle's longitudinal axis:

$$\begin{aligned} \beta_{fr} &= \arctan\left(\frac{a - R \sin \delta}{R \cos \delta + t_f/2}\right), & \beta_{fl} &= \arctan\left(\frac{a - R \sin \delta}{R \cos \delta - t_f/2}\right), \\ \beta_{fr} &= \alpha_{rr} = \arctan\left(\frac{b + R \sin \delta}{R \cos \delta + t_f/2}\right), & \beta_{fr} &= \alpha_{rl} = \arctan\left(\frac{b + R \sin \delta}{R \cos \delta - t_f/2}\right). \end{aligned} \quad (46)$$

d_1, d_2, d_3 , and d_4 are the force arms of the tire adhesive force about the vehicle's center of mass, respectively:

$$\begin{aligned} d_1 &= \sqrt{(t_f/2)^2 + a^2} \sin(\arctan \frac{t_f}{2a} + (\beta_{fr} + \alpha_{fr})), & d_2 &= \sqrt{(t_f/2)^2 + a^2} \cos(\arctan \frac{t_f}{2a} + (\beta_{fr} + \alpha_{fr})), \\ d_3 &= \sqrt{(t_f/2)^2 + a^2} \sin(\arctan \frac{t_f}{2a} - (\beta_{fr} + \alpha_{fr})), & d_4 &= \sqrt{(t_f/2)^2 + a^2} \cos(\arctan \frac{t_f}{2a} - (\beta_{fr} + \alpha_{fr})). \end{aligned} \quad (47)$$

Once we have the above relationships, we define a state variable as:

$$\mathbf{x} = [x, y, \psi, v]^\top, \quad (48)$$

where,

$$\dot{x} = v \cos(\psi), \quad (49)$$

$$\dot{y} = v \sin(\psi), \quad (50)$$

$$\dot{\psi} = \omega = \frac{1}{I_z} \sum M_z = \frac{1}{I_z} [F_{x,fr} d_1 + F_{y,fr} d_2 - F_{x,fl} d_3 + F_{y,fl} d_4 + F_{x,rr} \frac{t_r}{2} - F_{y,rr} b - F_{x,rl} \frac{t_r}{2} - F_{y,rl} b], \quad (51)$$

$$\dot{v} = \frac{1}{m} \left(\sum F_u \cos(\psi) + \sum F_v \sin(\psi) \right). \quad (52)$$

It should be noted that the experimental setup is designed solely to validate the effectiveness of the proposed method; therefore, data from other perception sensors commonly used in autonomous driving are excluded from training. Furthermore, trajectory prediction here is not performed by generating an entire trajectory in one shot. Instead, the model predicts one future point at a time and uses that prediction as input for the next step. This setting is adopted to evaluate and compare the accumulation of prediction errors over time against other methods.

To verify the generalization ability across different vehicle models, we trained the model using data from multiple vehicle types (i.e., vehicles with distinct parameters) simultaneously. Additionally, due to the significant noise present in the vehicle chassis data, we have performed denoising on the raw data. The necessity of this denoising process is also discussed in Appendix A.8.6.

Table 9. Quantitative results with variance on tracking tasks.

Method	Downtown Driving			Rural Driving		
	$e_{x\&z\downarrow}$	$e_{\psi\downarrow}$	$e_{v_x\downarrow}$	$e_{x\&y\downarrow}$	$e_{\psi\downarrow}$	$e_{v_x\downarrow}$
EKF	6.602 \pm 1.980	6.930 \pm 1.705	5.476 \pm 1.628	6.179 \pm 1.372	6.241 \pm 1.524	5.512 \pm 1.208
FCN	9.567 \pm 2.891	7.977 \pm 2.060	14.284 \pm 5.179	9.623 \pm 3.034	6.606 \pm 2.706	10.972 \pm 3.167
ResNet	9.236 \pm 2.769	6.899 \pm 1.592	9.094 \pm 2.772	5.517 \pm 0.989	10.361 \pm 2.974	9.315 \pm 1.601
PINN-FCN	8.824 \pm 1.062	14.488 \pm 2.965	17.287 \pm 3.907	8.279 \pm 1.291	10.349 \pm 1.352	15.251 \pm 3.740
PINN-ResNet	5.923 \pm 0.993	9.753 \pm 1.367	11.286 \pm 2.073	3.729 \pm 0.595	9.134 \pm 1.394	8.248 \pm 1.449
B-PINN	5.867 \pm 0.936	6.597 \pm 0.883	10.563 \pm 1.192	6.034 \pm 0.937	6.511 \pm 0.861	9.656 \pm 1.104
LSTM-RNN	8.953 \pm 1.392	10.199 \pm 1.495	11.298 \pm 2.968	9.643 \pm 1.420	8.831 \pm 1.631	8.168 \pm 1.093
LSTM-GA	9.019 \pm 1.022	6.579 \pm 0.846	8.442 \pm 0.781	9.005 \pm 1.923	5.994 \pm 0.821	10.837 \pm 1.907
DDPM	9.653 \pm 0.911	6.109 \pm 0.693	4.317 \pm 0.404	4.697 \pm 0.453	7.138 \pm 0.560	4.936 \pm 0.390
PIDM	4.845 \pm 0.721	4.733\pm0.458	5.671 \pm 0.437	4.293 \pm 0.502	5.874 \pm 0.483	4.061 \pm 0.469
PILD (Ours)	4.796\pm0.501	5.391 \pm 0.359	3.048\pm0.296	3.562\pm0.304	5.837\pm0.306	3.033\pm0.289

A.8.2. TIRE FORCE

Tire dynamic load refers to the dynamic vertical force exerted on the tire during vehicle motion. Due to the complexity of the vehicle chassis structure (incorporating components such as springs and dampers), directly calculating this load based solely on vehicle body attitude and acceleration introduces significant errors. This approach fails to accurately reflect the actual force experienced by the tire, thereby limiting the ability to properly evaluate chassis performance.

During vehicle operation, the spring & damper assembly undergoes expansion and contraction in response to relative displacement between the road surface and vehicle body. Since suspensions typically consist of multiple connecting rods forming complex single-degree-of-freedom (1DOF) or two-degree-of-freedom (2DOF) structures, suspension geometric parameters change dynamically during driving. A photograph of the actual suspension system is shown in Figure 10.

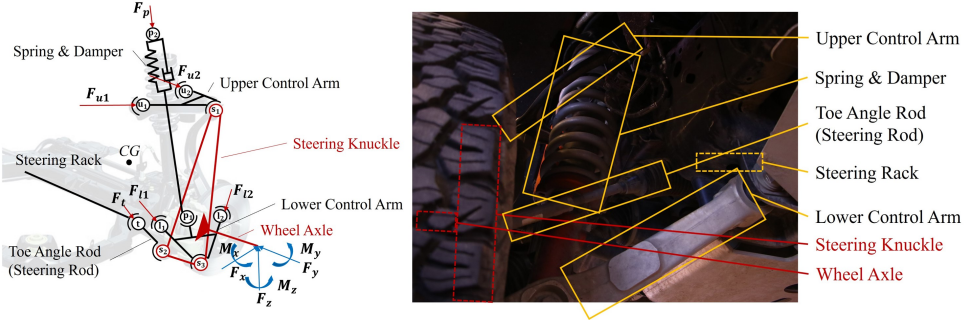


Figure 10. Physical suspension system.

Taking a double-wishbone suspension as an example, we simplify it to the linkage structure shown in Figure 10, comprising rods, ball joints, a spring, and a damper. The red component in the figure represents the steering knuckle, which connects directly to the wheel. Blue forces and moments indicate forces transmitted from the wheel to the suspension, while red forces represent internal forces within suspension rods.

For computational simplicity, we neglect the mass of individual suspension links, considering only the masses of the wheels and steering knuckles. Suspension hinge points are referred to as hard points, whose coordinates (for those not fixed to the vehicle body) change during driving. We define the hard points as follows: u_1 and u_2 (front and rear points of the upper control arm, UCA); l_1 and l_2 (front and rear points of the lower control arm, LCA); p_1 and p_2 (lower and upper joints of the spring-damper assembly); t (hinge joint between the steering knuckle and steering rack); s_1 , s_2 , and s_3 (upper, front, and lower points of the steering knuckle).

Here, CG denotes the center of mass; F_p , F_{u1} , F_{u2} , F_t , F_{l1} , F_{l2} represent suspension force vectors; F_x , F_y , F_z are tire forces transmitted from the wheel; and M_x , M_y , M_z are moments about the wheel axle.

We define the vector from CG to hard point i as \vec{i} (e.g., $\vec{u_1}$) and the direction vector from hard point i to j as \vec{ij} (e.g., $\vec{u_1s_1}$). Force vectors can thus be expressed as:

$$\begin{aligned} \mathbf{F}_p &= F_p \cdot \overrightarrow{\mathbf{p}_2 \mathbf{p}_1}, & \mathbf{F}_{u1} &= F_{u1} \cdot \overrightarrow{\mathbf{u}_1 \mathbf{s}_1}, & \mathbf{F}_{u2} &= F_{u2} \cdot \overrightarrow{\mathbf{u}_2 \mathbf{s}_1}, \\ \mathbf{F}_t &= F_t \cdot \overrightarrow{\mathbf{t} \mathbf{s}_2}, & \mathbf{F}_{l1} &= F_{l1} \cdot \overrightarrow{\mathbf{l}_1 \mathbf{s}_3}, & \mathbf{F}_{l2} &= F_{l2} \cdot \overrightarrow{\mathbf{l}_2 \mathbf{s}_3}, \end{aligned} \quad (53)$$

where unbolded coefficients represent scalar magnitudes of the corresponding forces. The suspension force matrix is:

$$\mathbf{F}_{\text{sus}} = [\mathbf{F}_p, \mathbf{F}_{u1}, \mathbf{F}_{u2}, \mathbf{F}_t, \mathbf{F}_{l1}, \mathbf{F}_{l2}] \quad (54)$$

Moments of these forces about CG are calculated as:

$$\begin{aligned} \mathbf{M}_p &= \overrightarrow{\mathbf{p}_2} \times \mathbf{F}_p, & \mathbf{M}_{u1} &= \overrightarrow{\mathbf{u}_1} \times \mathbf{F}_{u1}, & \mathbf{M}_{u2} &= \overrightarrow{\mathbf{u}_2} \times \mathbf{F}_{u2}, \\ \mathbf{M}_t &= \overrightarrow{\mathbf{t}} \times \mathbf{F}_t, & \mathbf{M}_{l1} &= \overrightarrow{\mathbf{l}_1} \times \mathbf{F}_{l1}, & \mathbf{M}_{l2} &= \overrightarrow{\mathbf{l}_2} \times \mathbf{F}_{l2}. \end{aligned} \quad (55)$$

The moment matrix is:

$$\mathbf{M}_{\text{sus}} = [\mathbf{M}_p, \mathbf{M}_{u1}, \mathbf{M}_{u2}, \mathbf{M}_t, \mathbf{M}_{l1}, \mathbf{M}_{l2}] . \quad (56)$$

Force and moment equilibrium relationships yield:

$$\sum_{i \in \{p, u1, u2, t, l1, l2\}} \mathbf{F}_i = \sum_{j \in \{x, y, z\}} \mathbf{F}_j, \quad \sum_{i \in \{p, u1, u2, t, l1, l2\}} \mathbf{M}_i = \sum_{j \in \{x, y, z\}} \mathbf{M}_j. \quad (57)$$

As shown in Figure 10, the front suspension has two degrees of freedom: steering and bump. We denote the steering rack displacement as x_a and the spring-damper expansion/contraction as x_d , both measurable by sensors. These parameters directly influence suspension geometry, so hard point coordinates are expressed as functions of x_a and x_d (e.g., $\overrightarrow{\mathbf{u}_1(x_a, x_d)}$, $\overrightarrow{\mathbf{u}_2(x_a, x_d)}$).

With a displacement sensor installed on the spring-damper assembly, \mathbf{F}_p can be determined as:

$$\mathbf{F}_p(t) = m \cdot f \left(\frac{\partial^2 x_d(t)}{\partial t^2} \right) + c \cdot \frac{\partial x_d(t)}{\partial t} + k \cdot x_d(t), \quad (58)$$

where $f \left(\frac{\partial^2 x_d(t)}{\partial t^2} \right)$ represents the nonlinear function of unsprung mass m acceleration acting on the spring-damper assembly, accounting for inertial forces.

According to the tire model, both \mathbf{F}_x and \mathbf{F}_y can be expressed by \mathbf{F}_z as:

$$\begin{aligned} F_y(\alpha, F_z, T) &= D(T) \sin[C(T) \arctan(B(T)\alpha - E(T)(B(T)\alpha - \arctan(B(T)\alpha)))] , \\ F_x(k, F_z, T) &= D_x(T) \sin[C_x(T) \arctan(B_x(T)s - E_x(T)(B_x(T)s - \arctan(B_x(T)s)))] , \end{aligned} \quad (59)$$

where, α is the slip angle, s is the longitudinal slip ratio; $B(T)$, $C(T)$, $D(T)$, $E(T)$ are temperature-dependent coefficients for lateral forces; $B_x(T)$, $C_x(T)$, $D_x(T)$, $E_x(T)$ are temperature-dependent coefficients for longitudinal forces; T represents tire temperature, which significantly affects rubber compound properties.

The peak force coefficient $D(T)$ exhibits strong temperature dependence, modeled as:

$$D(T) = F_z \cdot \mu(T) = F_z \cdot (a_0 + a_1 T + a_2 T^2 + a_3 \exp(-a_4 T)), \quad (60)$$

where $\mu(T)$ is the temperature-dependent friction coefficient, and a_0, \dots, a_4 are empirical parameters determined through tire testing. This relationship captures the reduction in friction with increasing temperature due to rubber hysteresis effects.

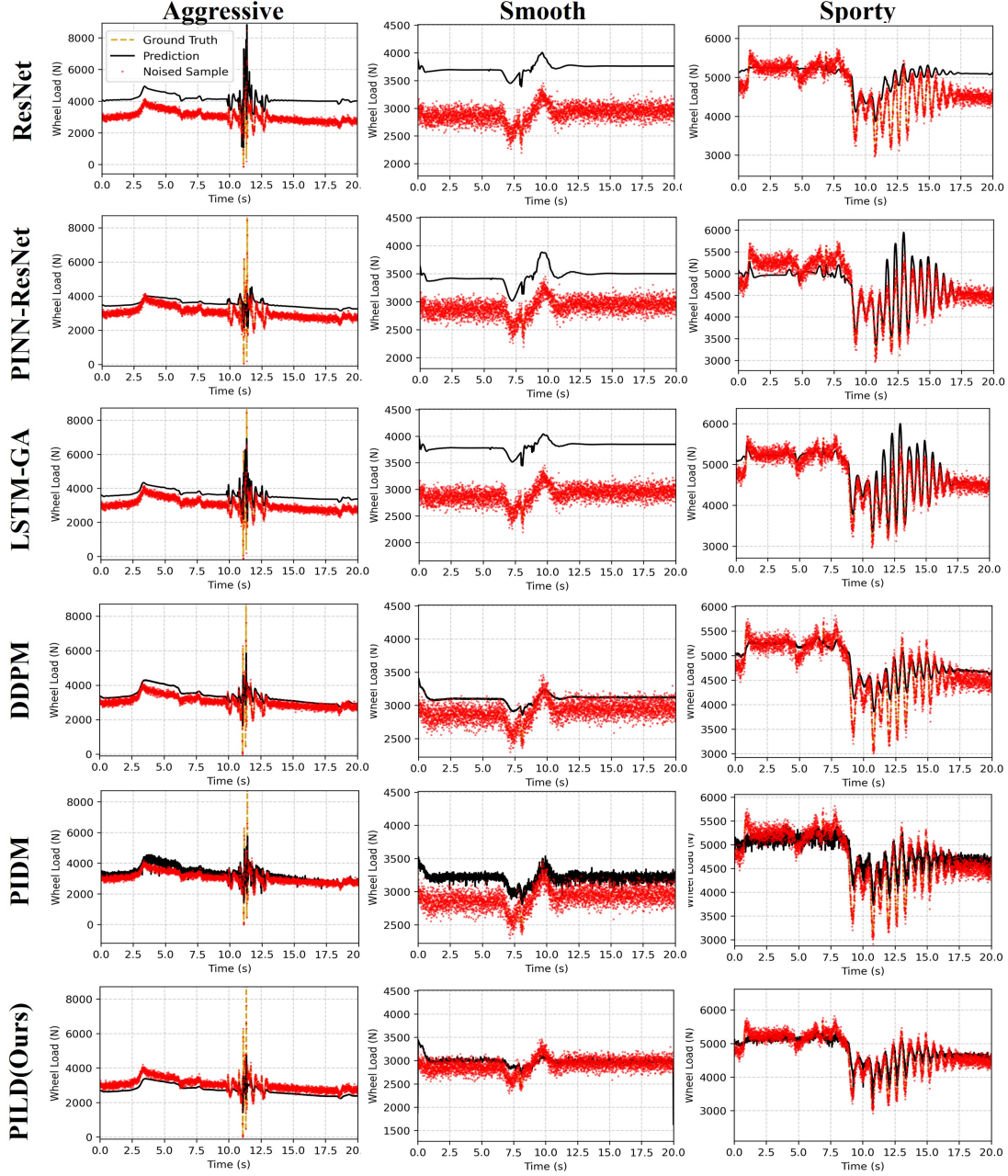


Figure 11. Experiment results on tire force estimation tasks.

Similarly, the longitudinal peak coefficient $D_x(T)$ follows the temperature-dependent relationship:

$$D_x(T) = F_z \cdot (c_0 + c_1 T + c_2 T^2 + c_3 \exp(-c_4 T)), \quad (61)$$

where c_0, \dots, c_4 are empirical parameters for longitudinal friction, determined through tire testing.

To derive the partial differential equation (PDE) governing wheel load $F_z(t, T)$ (with t as time and T as measured tire temperature), we start by substituting the tire force expressions into the equilibrium equations and considering dynamic variations.

From the force equilibrium, resolve the three-dimensional force balance into scalar components:

$$\sum_{i \in \{p, u1, u2, t, l1, l2\}} F_{i,x} = F_x(F_z, T, s), \quad \sum_{i \in \{p, u1, u2, t, l1, l2\}} F_{i,y} = F_y(F_z, T, \alpha), \quad \sum_{i \in \{p, u1, u2, t, l1, l2\}} F_{i,z} = F_z. \quad (62)$$

The left-hand sides of Equations of F_x and F_y depend on suspension geometry, which is a function of spring-damper compression $x_d(t)$. Using the chain rule, their time derivatives become:

$$\frac{d}{dt} \left(\sum F_{i,x} \right) = \sum \left(\frac{\partial F_{i,x}}{\partial x_d} \cdot \frac{\partial x_d}{\partial t} + \frac{\partial F_{i,x}}{\partial \dot{x}_d} \cdot \frac{\partial^2 x_d}{\partial t^2} \right), \quad (63a)$$

$$\frac{d}{dt} \left(\sum F_{i,y} \right) = \sum \left(\frac{\partial F_{i,y}}{\partial x_d} \cdot \frac{\partial x_d}{\partial t} + \frac{\partial F_{i,y}}{\partial \dot{x}_d} \cdot \frac{\partial^2 x_d}{\partial t^2} \right), \quad (63b)$$

where $\dot{x}_d = \partial x_d / \partial t$ and $\ddot{x}_d = \partial^2 x_d / \partial t^2$ are the velocity and acceleration of the spring & damper assembly, respectively.

The right-hand sides of Equations of F_x and F_y depend on F_z and T (measured as $T(t)$). Their total derivatives with respect to time are:

$$\frac{dF_x}{dt} = \frac{\partial F_x}{\partial F_z} \cdot \frac{\partial F_z}{\partial t} + \frac{\partial F_x}{\partial T} \cdot \frac{dT}{dt}, \quad \frac{dF_y}{dt} = \frac{\partial F_y}{\partial F_z} \cdot \frac{\partial F_z}{\partial t} + \frac{\partial F_y}{\partial T} \cdot \frac{dT}{dt}, \quad (64)$$

where $\partial F_x / \partial F_z$ and $\partial F_x / \partial T$ are partial derivatives of the longitudinal force with respect to vertical load and temperature, derived from the Pacejka Magic Formula (Equations (59)).

Equating the time derivatives from suspension dynamics and tire forces, then solving for $\partial F_z / \partial t$ yields the coupled PDE:

$$\frac{\partial F_z(t, T)}{\partial t} = \left[\left(\frac{\partial F_x}{\partial F_z} \right)^2 + \left(\frac{\partial F_y}{\partial F_z} \right)^2 \right]^{-1} \cdot \left\{ \frac{\partial F_x}{\partial F_z} \left[\sum \left(\frac{\partial F_{i,x}}{\partial x_d} \dot{x}_d + \frac{\partial F_{i,x}}{\partial \dot{x}_d} \ddot{x}_d \right) - \frac{\partial F_x}{\partial T} \dot{T} \right] \right. \\ \left. + \frac{\partial F_y}{\partial F_z} \left[\sum \left(\frac{\partial F_{i,y}}{\partial x_d} \dot{x}_d + \frac{\partial F_{i,y}}{\partial \dot{x}_d} \ddot{x}_d \right) - \frac{\partial F_y}{\partial T} \dot{T} \right] \right\}, \quad (65)$$

where $\dot{T} = dT / dt$ is the time rate of change of measured tire temperature.

This PDE explicitly captures: (1) **Time dependence** through spring-damper dynamics ($x_d, \dot{x}_d, \ddot{x}_d$) from suspension motion, (2) **Temperature dependence** through measured T and its rate \dot{T} , which modify tire friction coefficients, (3) **Coupling** between vertical load F_z and horizontal forces F_x, F_y via the Pacejka model derivatives.

Therefore, there are only six unknown quantities left in the entire system (force magnitudes $F_p, F_{u1}, F_{u2}, F_t, F_{l1}, F_{l2}$). With the six-dimensional equilibrium equations for force balance and moment balance (Equation (57)), combined with the derived PDE for $F_z(t, T)$, the problem is ultimately solved.

Table 10. Quantitative results with variance on tire force estimation tasks.

Method	Aggressive $e_F \downarrow$	Smooth $e_F \downarrow$	Sporty $e_F \downarrow$
EKF	1008.127 \pm 213.478	597.363 \pm 89.737	716.543 \pm 95.104
FCN	1257.633 \pm 221.739	601.559 \pm 98.712	794.780 \pm 102.563
ResNet	1121.367 \pm 204.319	585.561 \pm 79.301	647.976 \pm 98.417
PINN-FCN	1012.849 \pm 205.850	551.508 \pm 81.638	654.644 \pm 110.379
PINN-ResNet	994.783 \pm 178.662	642.110 \pm 78.361	653.944 \pm 95.558
B-PINN	1002.531 \pm 153.297	598.617 \pm 80.336	661.279 \pm 91.676
LSTM-RNN	1302.589 \pm 228.605	720.567 \pm 132.814	788.163 \pm 140.387
LSTM-GA	1150.434 \pm 219.348	582.840 \pm 96.622	642.638 \pm 102.228
DDPM	980.328 \pm 142.894	560.796 \pm 63.707	660.897 \pm 75.630
PIDM	988.642 \pm 150.277	579.546 \pm 57.095	630.543 \pm 85.367
PILD (Ours)	958.578\pm146.653	520.631\pm51.683	607.274\pm92.531

To verify the generalization ability across different vehicle models, we shuffled data from various vehicle types to construct the training and test datasets. More experimental results are demonstrated in Figure 11.

A.8.3. Darcy Flow

Darcy flow describes the seepage behavior of fluids in porous media and serves as a canonical benchmark for validating physics-constrained generative models. This section presents an overview of its core theoretical components, including the governing equations, numerical solution approach, and dataset construction.

The flow of incompressible fluids through porous media is governed by Darcy's law and the principle of mass conservation, which together form the following partial differential equation (PDE):

$$-\nabla \cdot (K(\mathbf{x}) \nabla p(\mathbf{x})) = f_s(\mathbf{x}), \quad \mathbf{x} \in \Omega \subset \mathbb{R}^2, \quad (66)$$

where $p(\mathbf{x})$ is the pressure field, $K(\mathbf{x})$ is the spatially-varying permeability field that characterizes the medium's conductivity, and $f_s(\mathbf{x})$ is a prescribed source/sink term (modeling fluid injection or extraction). The domain Ω is typically taken as the unit square $[0, 1]^2$. This system is subject to homogeneous Neumann boundary conditions ($\nabla p \cdot \mathbf{n} = 0$ on $\partial\Omega$), representing no-flow boundaries, and a zero-mean pressure constraint ($\int_{\Omega} p(\mathbf{x}) d\mathbf{x} = 0$) to ensure solution uniqueness.

The fluid velocity field $\mathbf{u}(\mathbf{x})$ is related to the pressure gradient via Darcy's law:

$$\mathbf{u}(\mathbf{x}) = -K(\mathbf{x}) \nabla p(\mathbf{x}). \quad (67)$$

This constitutive relation implies that fluid flows from regions of high pressure to low pressure, with the local flux being modulated by the permeability of the medium at that point. In practice, the velocity field is often not directly used as a model output; instead, it can be post-processed from the pressure solution using finite difference approximations of the gradient.

In the standard benchmark setup adopted from prior work such as CoCoGen (Jacobsen et al., 2025), the source term $f_s(\mathbf{x})$ is fixed to a constant value across all samples (e.g., $f_s \equiv 1$), thereby isolating the effect of the heterogeneous permeability field $K(\mathbf{x})$ on the resulting pressure distribution. The permeability field itself is generated stochastically: it is obtained by applying an exponential transform to a random field with a specified correlation length (typically $\ell = 0.1$ or 0.2). This ensures that $K(\mathbf{x})$ remains strictly positive (a physical requirement) while exhibiting spatially correlated structures that mimic real geological formations.

To construct the dataset, the continuous PDE is discretized on a uniform Cartesian grid of size $s \times s$, where $s = 64$ is the resolution. At each grid node (i, j) , the spatial coordinate is given by $\mathbf{x}_{i,j} = ((i-1)/(s-1), (j-1)/(s-1))^T$. A linear system $\mathbf{A}\mathbf{p} = \mathbf{f}$ is then assembled using second-order finite differences to approximate the divergence and gradient operators in the PDE. Solving this sparse linear system yields the discrete pressure values $\{p_{i,j}\}$ at all grid points, forming the field $p(\mathbf{x})$.

Consequently, each training instance consists of a paired sample $\{K(\mathbf{x}), p(\mathbf{x})\}$, where both fields are represented as $s \times s$ images. The mapping from permeability to pressure is highly non-linear and non-local, making it a challenging inverse problem and an excellent testbed for evaluating a generative model's ability to capture complex physical dependencies.

In this experiment, both the horizontal and vertical coordinates range from 0 to 64, corresponding to 64 pixels. The training and test datasets are generated via numerical simulation. Figure 12 demonstrates more samples of the experiment.

A.8.4. Plasma Dynamics

Low-temperature, magnetized plasmas in the edge region of tokamaks (e.g., scrape-off layer, pedestal) exhibit inherently complex turbulent behavior driven by instabilities such as drift waves, resistive interchange modes, and blob propagation (Greenwald et al., 2014; LaBombard et al., 2005), which govern particle and energy transport, wall loading, and pedestal stability—critical factors for the viability of magnetic confinement fusion reactors. A widely adopted theoretical framework for simulating this regime is the drift-reduced Braginskii model (Fitzpatrick, 2022), which provides a set of coupled fluid equations describing the evolution of key plasma quantities (density, temperature, velocity, electrostatic potential) while retaining essential physics of magnetized collisional plasmas. This work establishes a benchmark model focused on the dynamics of electron density $n_e(\mathbf{x}, t)$ and electron temperature $T_e(\mathbf{x}, t)$ —fields directly measurable via diagnostics (e.g., gas puff imaging (Zweben et al., 2017), Langmuir probes) and central to characterizing edge turbulence—by deriving the normalized two-dimensional (2D) model from the full 3D drift-reduced Braginskii equations, detailing key approximations, and specifying numerical parameters consistent with tokamak edge experiments.

The drift-reduced Braginskii model is derived under core assumptions including the low- β condition (plasma pressure negligible compared to magnetic pressure, justifying the electrostatic approximation $\mathbf{B} = B_0 \hat{\mathbf{z}}$), magnetized species (ion

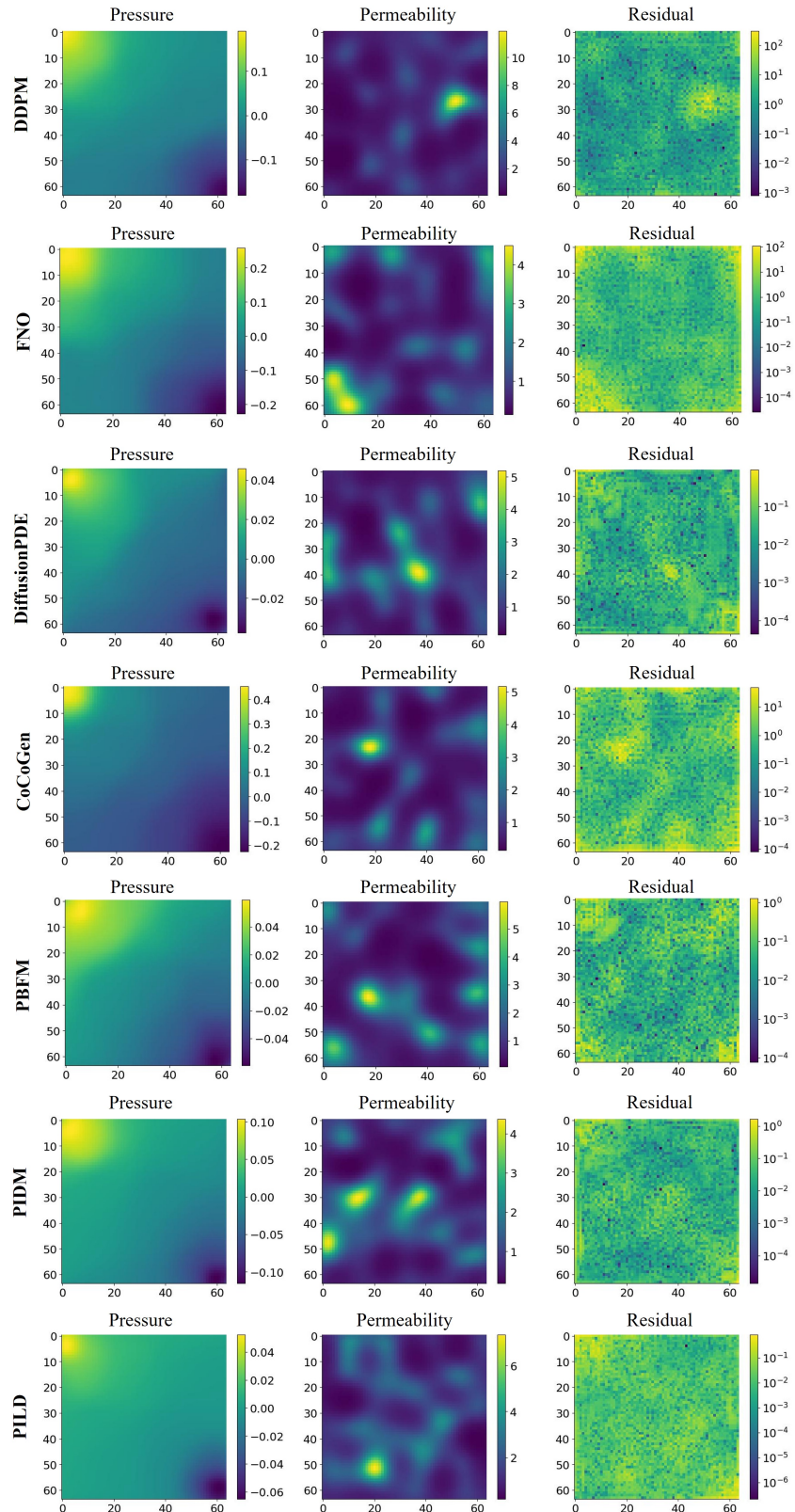


Figure 12. Experiment results on Darcy flow generation.

gyration frequency $\Omega_i \gg$ turbulent fluctuation frequency $\partial/\partial t$, allowing neglect of ion inertia in perpendicular dynamics), quasineutrality ($n_e \approx n_i = n$, no local charge imbalance with $\nabla \cdot \mathbf{j} = 0$), and the collisionless limit for edge plasmas (collisional drifts and viscosity negligible compared to drift-wave dynamics, except for diffusive losses). The 3D evolution equations for electron density n_e and electron temperature T_e (in physical units) are given by:

$$\frac{d^e n_e}{dt} = -\frac{2c}{B_0} \left[n_e C_{(\phi)} - \frac{1}{e} C_{(p_e)} \right] - n_e \nabla_{\parallel} v_{\parallel e} + S_n + \mathcal{D}_{n_e}, \quad (68)$$

$$\frac{d^e T_e}{dt} = -\frac{5}{3} \frac{T_e}{n_e} \nabla_{\parallel} v_{\parallel e} + \frac{2}{3n_e} \nabla_{\parallel} \left(\kappa_{\parallel}^e \nabla_{\parallel} T_e \right) + \frac{1}{n_e} S_{E,e} + \mathcal{D}_{T_e}, \quad (69)$$

where $d^e f/dt = \partial_t f + (c/B_0)[\phi, f] + v_{\parallel e} \nabla_{\parallel} f$ is the species-convective derivative for electrons accounting for $\mathbf{E} \times \mathbf{B}$ drift ($\mathbf{E} = -\nabla\phi$) and parallel advection, $[\phi, f] = b_0 \times \nabla\phi \cdot \nabla f$ is the Poisson bracket (2D projection of $\mathbf{E} \times \mathbf{B}$ drift advection with $b_0 = \hat{\mathbf{z}}$), $C_{(f)} = b_0 \times \kappa \cdot \nabla f$ is the curvature operator ($\kappa = -\dot{R}/R$, tokamak major radius R , negligible in slab geometry for benchmarking), $p_e = n_e T_e$ is electron pressure (Boltzmann relation for ideal plasma), $\nabla_{\parallel} = \partial/\partial z$ is the parallel gradient, $v_{\parallel e}$ is parallel electron velocity, κ_{\parallel}^e is parallel thermal conductivity, S_n ($\text{m}^{-3}\text{s}^{-1}$) and $S_{E,e}$ ($\text{eVm}^{-3}\text{s}^{-1}$) are particle and energy sources, and \mathcal{D}_{n_e} and \mathcal{D}_{T_e} are diffusive terms (cross-field and parallel diffusion, dominated by anomalous transport in edge plasmas).

To simplify numerical implementation and ensure physical consistency, all variables are normalized using reference scales derived from tokamak edge parameters: reference density $n_0 = 5 \times 10^{19} \text{ m}^{-3}$, reference temperature $T_0 = 25 \text{ eV}$, reference potential $\phi_0 = T_0/e$, reference length $a_0 = 0.22 \text{ m}$, and reference time $t_0 = a_0/v_{E0}$ (with $v_{E0} = \phi_0/(B_0 a_0)$ as characteristic $\mathbf{E} \times \mathbf{B}$ drift velocity, $B_0 = 5 \text{ T}$). Normalized quantities are defined as:

$$\tilde{n}_e = \frac{n_e}{n_0}, \quad \tilde{T}_e = \frac{T_e}{T_0}, \quad \tilde{\phi} = \frac{\phi}{\phi_0}, \quad \tilde{x} = \frac{x}{a_0}, \quad \tilde{t} = \frac{t}{t_0},$$

with normalized operators $\tilde{\nabla} = a_0 \nabla$, $\tilde{\nabla}_{\perp}^2 = a_0^2 \nabla_{\perp}^2$, and $[\tilde{f}, \tilde{g}] = a_0^2 [f, g]_{\text{physical}}$. Substituting these into the 3D equations and simplifying—neglecting parallel advection terms due to slow z -direction variation ($\tilde{\nabla}_{\parallel} \rightarrow 0$, 2D slab approximation), curvature terms in slab geometry, approximating diffusive terms as anomalous cross-field diffusion, and adding damping terms to model particle/energy losses to the wall—yields the normalized 2D equations for \tilde{n}_e and \tilde{T}_e :

$$\frac{\partial \tilde{n}_e}{\partial \tilde{t}} + [\tilde{\phi}, \tilde{n}_e] = D_n \tilde{\nabla}_{\perp}^2 \tilde{n}_e - \alpha_n (\tilde{n}_e - 1) + \tilde{S}_n, \quad (70)$$

$$\frac{3}{2} \frac{\partial \tilde{T}_e}{\partial \tilde{t}} + \frac{3}{2} [\tilde{\phi}, \tilde{T}_e] + \frac{1}{2} [\tilde{\phi}, \tilde{n}_e] = D_T \tilde{\nabla}_{\perp}^2 \tilde{T}_e - \alpha_T (\tilde{T}_e - 1) + \tilde{S}_T. \quad (71)$$

In these equations, the time derivative terms capture the temporal evolution of density and temperature, with the factor $3/2$ for temperature originating from the thermal energy of a monatomic gas ($U = \frac{3}{2}nT$). The $\mathbf{E} \times \mathbf{B}$ advection terms, defined via the Poisson bracket $[\tilde{\phi}, \tilde{f}] = \partial_x \tilde{\phi} \partial_y \tilde{f} - \partial_y \tilde{\phi} \partial_x \tilde{f}$, describe turbulent transport driven by the electric drift velocity, while the coupled advection term $\frac{1}{2}[\tilde{\phi}, \tilde{n}_e]$ in the temperature equation accounts for energy transport correlated with density gradients (derived from parallel heat flux closure). The anomalous diffusion terms $D_n \tilde{\nabla}_{\perp}^2 \tilde{n}_e$ and $D_T \tilde{\nabla}_{\perp}^2 \tilde{T}_e$ model cross-field transport from turbulent eddies, with D_n and D_T as anomalous diffusion coefficients, and the wall damping terms $-\alpha_n (\tilde{n}_e - 1)$ and $-\alpha_T (\tilde{T}_e - 1)$ enforce linear relaxation to equilibrium (representing particle and energy losses to tokamak walls). The source terms \tilde{S}_n and \tilde{S}_T correspond to external particle injection (e.g., gas puff) or energy input (e.g., radiofrequency heating).

The electrostatic potential $\tilde{\phi}$ is determined self-consistently via quasi-neutrality, with the simplified Boltzmann approximation $\tilde{\phi} \approx \tilde{n}_e$ adopted for the benchmark model—valid for low-temperature edge plasmas and sufficient to close the system. For higher fidelity, the full quasi-neutrality condition $\nabla_{\perp}^2 \tilde{\phi} = \tilde{n}_e - \tilde{n}_i$ can be employed, though the Boltzmann approximation adequately captures core turbulent dynamics such as blob propagation.

The numerical setup for synthetic dataset generation is consistent with the global drift-ballooning (GDB) code and tokamak experiments: the 2D poloidal simulation domain spans physical dimensions $x \in [0, 3.8 \text{ cm}]$ and $y \in [0, 3.8 \text{ cm}]$ (normalized $\tilde{x}, \tilde{y} \in [0, 0.173]$) with grid resolution $\Delta \tilde{x} \approx 1.36 \times 10^{-3}$ and $\Delta \tilde{y} \approx 1.82 \times 10^{-3}$. Boundary conditions include homogeneous Neumann conditions for \tilde{n}_e and \tilde{T}_e (no net flux at domain edges) and a Dirichlet condition $\tilde{\phi} = 0$ at boundaries (enforcing radial $\mathbf{E} \times \mathbf{B}$ drift to zero). Initial conditions are truncated Gaussian profiles:

$$\tilde{n}_e(\tilde{x}, \tilde{y}, 0) = 1 + 0.2 \exp \left(-\frac{\tilde{x}^2 + \tilde{y}^2}{2\sigma^2} \right), \quad \tilde{T}_e(\tilde{x}, \tilde{y}, 0) = 1 + 0.15 \exp \left(-\frac{\tilde{x}^2 + \tilde{y}^2}{2\sigma^2} \right),$$

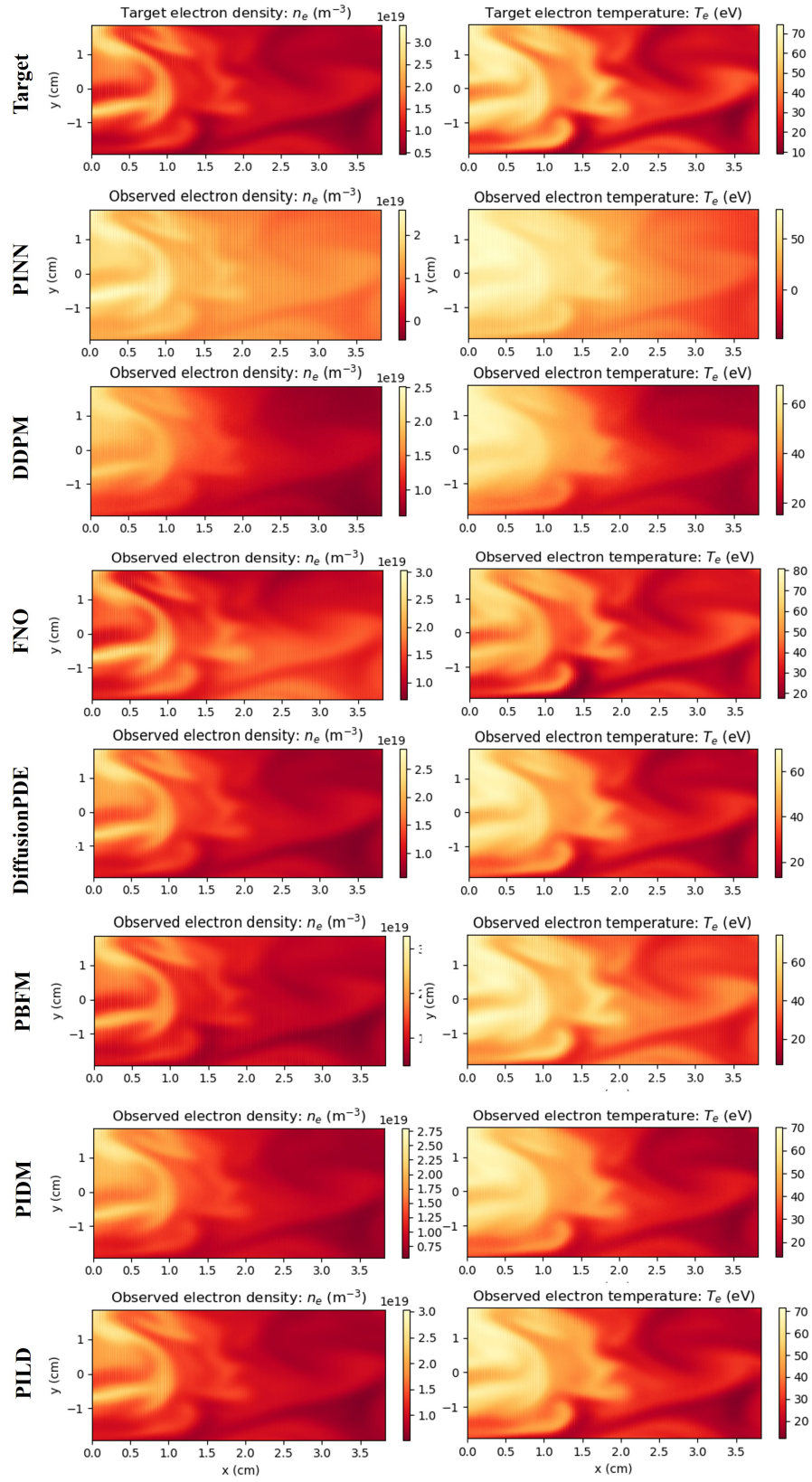


Figure 13. Experiment results on plasma dynamics prediction.

where $\sigma = 0.05$ (normalized width, corresponding to ≈ 1 cm physical width). Benchmark parameters calibrated to edge plasma turbulence are $D_n = 1.0 \times 10^{-4}$, $D_T = 1.5 \times 10^{-4}$, $\alpha_n = 0.1 \tilde{t}^{-1}$, $\alpha_T = 0.08 \tilde{t}^{-1}$, $\tilde{S}_n = 0.05$, and $\tilde{S}_T = 0.03$.

The system is solved using a second-order finite difference method with a trapezoidal leap-frog time integration scheme, implicit integration of diffusion terms (to avoid numerical instability from stiff diffusion), and a normalized time step $\Delta \tilde{t} = 1.0 \times 10^{-3}$ (corresponding to $\approx 4.55 \times 10^{-11}$ s physical time, consistent with the GDB code). This setup reproduces key edge plasma phenomena observed in experiments and full 3D simulations (Mathews et al., 2021), including blob propagation (filamentary structures advected radially outward via $\mathbf{E} \times \mathbf{B}$ drift), turbulent transport (anomalous diffusion coefficients matching measured cross-field transport levels), and coupled density-temperature dynamics.

For PINNs, the residuals of Eqs. (70) and (71) serve as regularization to ensure learned models satisfy physical constraints even with partial or noisy observations:

$$\begin{aligned}\mathcal{R}_{\tilde{n}_e} &= \frac{\partial \tilde{n}_e}{\partial \tilde{t}} + [\tilde{\phi}, \tilde{n}_e] - D_n \tilde{\nabla}_\perp^2 \tilde{n}_e + \alpha_n (\tilde{n}_e - 1) - \tilde{S}_n, \\ \mathcal{R}_{\tilde{T}_e} &= \frac{3}{2} \frac{\partial \tilde{T}_e}{\partial \tilde{t}} + \frac{3}{2} [\tilde{\phi}, \tilde{T}_e] + \frac{1}{2} [\tilde{\phi}, \tilde{n}_e] - D_T \tilde{\nabla}_\perp^2 \tilde{T}_e + \alpha_T (\tilde{T}_e - 1) - \tilde{S}_T.\end{aligned}$$

The benchmark can be extended to toroidal geometry by reinstating curvature terms $C_{(f)} = -\frac{1}{R_0} \partial_y f$ (where $R_0 = 0.68$ m is the tokamak major radius (Greenwald et al., 2014)) and modifying the Poisson bracket to:

$$[\tilde{\phi}, \tilde{f}]_{\text{toroidal}} = \partial_x \tilde{\phi} \partial_y \tilde{f} - \partial_y \tilde{\phi} \partial_x \tilde{f} - \frac{1}{R_0} \partial_y \tilde{\phi} \partial_y \tilde{f},$$

which captures resistive interchange instabilities dominant in bad-curvature regions of tokamaks.

Due to the scarcity of plasma data, the experimental data in this case is also obtained through numerical simulation (Mathews et al., 2021). Figure 13 demonstrates some results of the experiment.

A.8.5. DESCRIPTION OF OTHER COMPARATIVE METHODS

The first two experimental scenarios are engineering application scenarios, where the comparative methods include common methods for the corresponding scenarios and methods of the same category as the proposed PILD in this paper. Specifically, the EKF is a traditional method widely used for state estimation in nonlinear engineering systems; the FCN and ResNet methods are classic neural network approaches that directly learn the mapping between input and output data; the two PINN-based methods incorporate physical loss terms into the aforementioned two neural network architectures, which is a commonly adopted practice in physics-informed neural networks for engineering systems; the B-PINN is characterized by Bayesian operations, enabling it to handle system noise; the two LSTM-based methods are designed for processing time-series data; and the DDPM and PIDM methods share a similar overall architecture with PILD, all belonging to diffusion-based approaches. These two sets of experiments truly reflect the scenarios of actual engineering systems. For fair comparison, we adapted various baseline methods: among them, open-source codes are available for LSTM-RNN, B-PINN, DDPM, and PIDM, while the other methods were reproduced based on their original papers. All models were fully trained to ensure fair comparison.

The latter two experiments correspond to scientific machine learning scenarios, where the comparative methods include common fluid processing approaches and several state-of-the-art diffusion-based methods. Specifically, DDPM and FNO, as classic methods for scientific machine learning tasks, are widely used in fields such as fluid mechanics and material mechanics, with corresponding open-source codes available. PINN and CoCoGen, originally serving as dataset providers, have demonstrated excellent performance on their respective tasks and offer detailed reproduction instructions. PBFM is a flow-matching-based method with open-source code, and it has been tested on the Darcy flow dataset and achieves good performance. DiffusionPDE and PIDM, as emerging physics-informed learning models based on diffusion architectures, have also achieved promising results across various datasets, including the classic fluid mechanics scenario of Darcy flow. All the aforementioned methods were adapted to our experimental settings: Darcy flow is inherently compatible with these methods, while plasma dynamics can also be accommodated by them in terms of data structure. All models were fully trained; for methods with provided pre-trained weights, we performed fine-tuning on these weights to ensure the effectiveness of the comparative methods.

A.8.6. ABLATION STUDIES

With or without denoising preprocessing. It should be noted that we evaluate the performance of different methods on real-world datasets with noise after applying denoising as a preprocessing step using Gaussian filtering (Ito & Xiong, 2002) in the main text. Here, the experiment demonstrates the performance of various methods on experimental inputs without any denoising applied. We conduct the experiment on the Tire Force dataset, and the results are reported in Table 11. It can be observed that denoising improves the performance of all methods to some extent. However, since denoising may suppress fine-grained features in the data, other approaches struggle to effectively reconcile physical models with the underlying data distribution. In contrast, PILD maintains superior performance, demonstrating its robustness and ability to jointly leverage physics and data characteristics.

Table 11. Ablation studies on input denoising by Gaussian filtering.

Method	Denoised Input	Original Input
PINN-ResNet	774.011	957.683
DDPM	763.612	781.054
PIDM	732.910	828.933
PILD(Ours)	695.494	775.914

We also select one group of samples generated with original noisy input without any preprocessing in Figure 14.

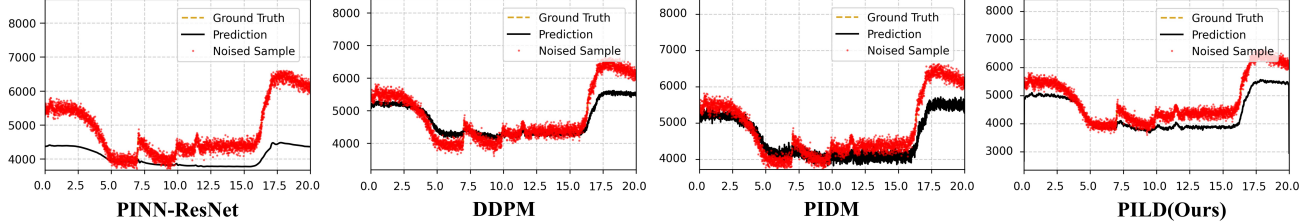


Figure 14. Ablation results with noisy input on Tire Force benchmark.

It should be noted that our model was trained on many different vehicle types simultaneously. After applying the original data noise, it can be observed that the PINN-Res has almost completely failed. Although the RMSE loss can achieve a denoising effect, the PINN-Res model has deviated too far from the target. Additionally, the PIDM failed to achieve complete denoising. In this sample, both DDPM and PILD achieved satisfactory performance: PILD denoised the data more thoroughly but introduced a larger deviation than DDPM. However, in terms of the overall test results, PILD was slightly superior. The presentation of this sample also illustrates the importance of data preprocessing.

Different gating functions. Here, we demonstrate the impact of different types of gating functions tested in our experiments on the experimental outcomes, with the primary effects lying in the convergence speed and the final accuracy. We use Darcy flow as the benchmark to illustrate the performance of different gating functions. The results are presented in Table 12.

Table 12. Ablation settings for gating function.

Gating function	Testing residual error	Testing data loss
w/o $G(t)$	8.635×10^{-3}	6.812×10^{-3}
$G_1(t) = 2 - \frac{t}{T}$	1.660×10^{-2}	6.745×10^{-3}
$G_2(t) = \frac{T}{1+t}$	3.179×10^{-3}	1.248×10^{-2}
$G_3(t) = \log(1 + \frac{T}{1+t})$	8.436×10^{-3}	5.763×10^{-3}

We select three forms of $G(t)$ representing distinct scheduling strategies: linear scheduling, inverse proportional scheduling, and logarithmic scheduling. Compared to the baseline without $G(t)$, only the logarithmic scheduling outperforms the baseline in both residual error and data loss. The linear scheduling $G_1(t)$, due to its narrow adjustment range, merely ensures the optimization of data loss. In contrast, the inverse proportional scheduling causes $G_2(t)$ to increase sharply as $t \rightarrow 0$, where the overwhelming influence of physical constraints disrupts the consistency of the data distribution, ultimately

leading to an increase in data loss. This leads the model's generated outputs to be confined to local optima with minimal physical residual loss, while in reality, they have deviated from the original data distribution. The logarithmic scheduling $G_3(t)$, however, balances the scheduling trends of the aforementioned two methods. It reduces residual error while lowering data loss without being overly aggressive, ultimately achieving a favorable trade-off between physical compliance and data fidelity.

Training cost. Our method provides two conditional embedding approaches: U-FiLM and U-Att.

Table 13. Ablation results of training cost.

Module used	Tracking	Plasma
U-FiLM	30min	10.5h
U-Att	35min	11.5h

U-FiLM trains slightly faster than U-Att and exhibits higher efficiency for low-dimensional data. Herein, we select a low-dimensional experiment (tracking) and a high-dimensional experiment (plasma) to illustrate the training time, with the results presented in Table 13.